THz Photomixers

Emilien Peytavit, Guillaume Ducournau, Jean-Francois Lampin

THz Photomixers

E. Peytavit, G. Ducournau, J-F. Lampin

Table of Contents

Introduction

This chapter is mainly focused on the generation of continuous waves in the THz frequency range by using the optical heterodyne, also called photomixing of two slightly detuned (of a frequency $\Delta\nu$), spatially overlapped, infrared laser beams in an ultrafast photodetector. We are not able to present exhaustively all the works which have been carried out in this field these last twenty years and we will focus on two standard photomixers devices: ultrafast photoconductors based on sub-picosecond carrier lifetime semiconductors (e.g. low-temperature grown GaAs, InGaAs:Fe, etc.) and uni-travelling-carrier InP/InGaAs photodiodes.

1 Photomixing Basics

1.1 Photomixing Principle

Let's assume two continuous-wave (cw) laser beams spatially overlapped of angular frequencies $\omega_1 = \omega_0 + \frac{1}{2}\omega_b$ and $\omega_2 = \omega_0 - \frac{1}{2}\omega_b$ and wave vectors having a same polarization (parallel to $\overrightarrow{e_y}$)

and magnitude. In a plane wave approximation and assuming that the direction of propagation of the lasers is alongthe z-axis, the electric field of one laser can be written as:

Eq. 1 $$\overrightarrow{E_i}(z,t) = E_0\cos(\omega_i t - k_i z)\overrightarrow{e_y} = E_0\cos(\omega_i t + \varphi_i(z))\overrightarrow{e_y}$$

The total electric field is then:

Eq. 2 $$\vec{E}(z,t) = E_0[\cos(\omega_1 t+\varphi_1) + \cos(\omega_2 t+\varphi_2)]\overrightarrow{e_y}$$

$$= 2E_0\left[\cos\left(\omega_0 t+\frac{1}{2}(\varphi_1+\varphi_2)\right)\cos\left(\frac{1}{2}\omega_b t+\frac{1}{2}(\varphi_1-\varphi_2)\right)\right]\overrightarrow{e_y}$$

We recognize here a carrier at angular frequency $\omega_0$modulated by an envelope at angular frequency $\frac{1}{2}\omega_b$

The energy flux density of the superposition of the two fields is then

Eq. 3 $$\vec{S}(z,t) = \vec{E}(z,t) \wedge \vec{H}(z,t) = y_0\left|\vec{E}(z,t)\right|^2\overrightarrow{e_z}$$

$$\left|\vec{S}(z,t)\right| = y_0\left|\vec{E}(z,t)\right|^2 = 4y_0{E_0}^2\cos^2\left(\omega_0 t+\frac{1}{2}(\varphi_1+\varphi_2)\right)\cos^2\left(\frac{1}{2}\omega_b t+\frac{1}{2}(\varphi_1-\varphi_2)\right)$$

$$= y_0{E_0}^2(1+cos(2\omega_0 t+(\varphi_1+\varphi_2))(1+cos(\omega_b t+(\varphi_1-\varphi_2))$$

where $y_0 = \frac{1}{Z_0} = (\varepsilon_0/\mu_0)^{1/2}$ is the admittance of free space.

In a photomixing experiment, the laser frequencies, ω_0 is far above the cut-off frequency of the photomixer, and only the time average (equal to zero) of its contribution is detected. The difference frequency $\omega_b = \omega_2 - \omega_1$is chosen small enough to be followed by the photodetector. The energy flux density detected by the photomixer is therefore

Eq. 4 $$\left|\vec{S}(z,t)\right| = y_0{E_0}^2[1+cos(\omega_b t+(\varphi_1-\varphi_2)] = S_0[1+cos(\omega_b t+(\varphi_1-\varphi_2)]$$

The detected energy flux density is composed of a dc part, which is the sum of the laser energy flux densities taken separately $\frac{1}{2}S_0 = \frac{1}{2}y_0{E_0}^2$, and a modulated part. The frequency ω_b of the modulation of the energy flux density is the frequency difference of the two lasers. ω_b can be easily tuned by tuning the frequency of at least one of both lasers. As the laser frequencies are much larger than ω_b, only a small relative tuning range of the laser is sufficient for the photomixer's output signal to be widely tunable. In practice, the tuning range is limited by the frequency limitation of the photomixer.

1.2 Historical Background

The first experimental demonstration of the mixing of two optical sources is shown in 1955 by T.A Forrester *et al.* with a photocathode illuminated by two zeeman components of an atomic spectral line separated by 10 GHz [1]. However, this technique has received a great deal of attention after the

appearance of the laser in 1960 providing sufficiently coherent and easy to use optical sources. The first optical mixing of laser sources is done in 1962 by A. Javan *et al.* [2] with two single mode He-Ne lasers mixed in the photocathode of a photomultiplier. The beating frequency is 5 MHz and is detected by a spectrum analyzer. The main goal of the experiment is actually the measurement of the spectral purity of the laser and not the generation of microwaves. In the same year, several reports of photomixing with beating frequencies lying in the GHz range follow this work, in which the photomixer is firstly a transparent cathode of a standard microwave traveling wave tube (TWT) [3]. Solid state photomixers appear in a second time, with the use of a p-i-n junction Germanium photodiode [4], [5] and a biased photoconductive CdSe crystal [6]. In these pioneering works, the optical sources consist of near longitudinal modes of a ruby laser or a He-Ne laser. Two years later, the physical and electrical model of the microwave generation by photomixing done by P.D Coleman *et al.* [7] give the key parameters for the optimisation of the generated power. In the 1990's, with the progress of solid-state lasers and high-speed photodetectors, the interest in the microwave generation by the optoelectronic route is revived. The first demonstration of THz generation by photomixing is reported in 1995 by E.R Brown *et al.* [8] thanks to an ultrafast photoconductor, consisting of an interdigitated electrode capacitance on a low-temperature-grown GaAs (LT-GaAs) and pumped by two Ti:Al_2O_3 lasers working around λ=0.8µm. The photomixer is coupled to a spiral antenna and the radiated THz waves are detected by a He-cooled bolometer. The LT-GaAs, discovered some years before [9], seems actually, to be a perfect semiconductor for ultrafast optoelectronics, due to a subpicosecond carrier lifetime, a high electric-field breakdown (~300 kV/cm) [10] combined with a relatively high electron mobility (~150 cm^2/Vs) [11]. The output power is quite low, i.e. 4 µW at 300 GHz and 1 µW at 800 GHz, but the noise level is reached only at 3.8 THz. The second breakthrough is achieved in 2003 by Ito *et al.* [12] with the report of ~80 µW at 300 GHz and 2.6 µW at 1 THz a with InP-based uni-travelling carrier photodiodes (UTC-PD) initially developed for telecom applications and pumped by 1.55-µm-wavelength lasers. As far as concern the output power, no significant improvements have been achieved since these two pioneer works.

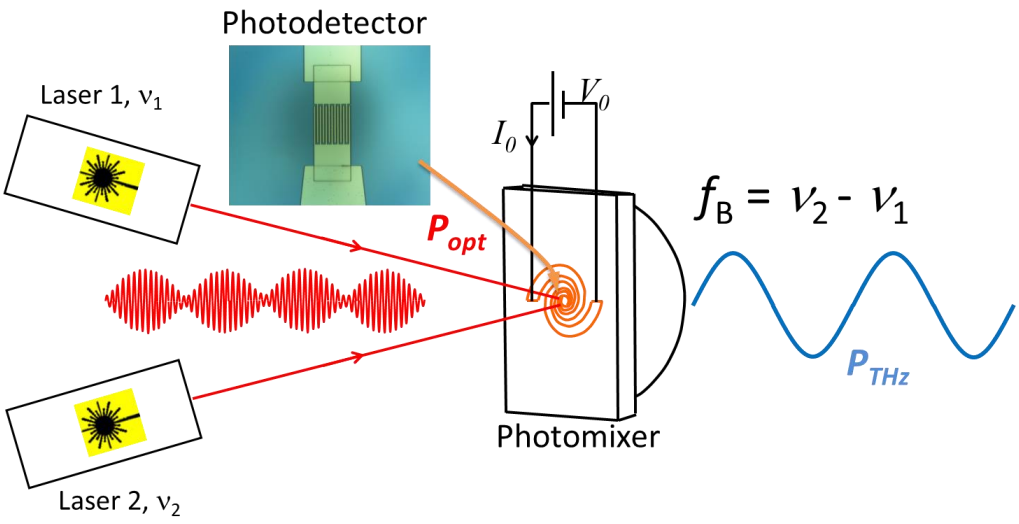

Figure 1: THz generation by photomixing

2 Modeling THz photomixers

The purpose of this section is the presentation of an electrical model of a THz source based on photomixing in photodetectors. This will be followed by an estimation of the level of power that can be generated by this method.

2.1 Photoconductors

2.1.1 Photocurrent Generation

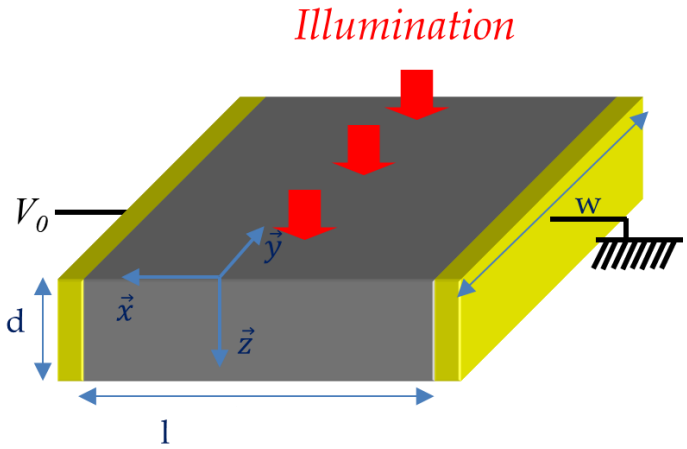

Figure 2: Photomixing in a photoconductor

As seen in the previous part, the incident energy flux density (or intensity) in a photomixing experiment can be written as:

Eq. 5 $$S(z,t) = \left|\vec{S}(z,t)\right| = S_0[1 + cos(\omega_b t + (\varphi_1(z) - \varphi_2(z))]$$

If we assume an illumination on the surface area of the photoconductor being at $z = 0$, the intensity of the light impinging the photoconductor can be written as:

Eq. 6 $$S_{z0}(t) = S(z = 0, t) = S_0[1 + cos(\omega_b t + \varphi)] \text{ where } \varphi = (\varphi_1(0) - \varphi_2(0))$$

A schematic of a photoconductor illuminated by an optical beatnote is shown in Figure 2. Here, we consider an ideal photoconductor of capacitance *C*, having a single type of carrier of mobility μ, a lifetime τ and a free carrier density n_{dark} assumed to be zero. When the energy flux density impinges the photoconductor, a fraction $(1 - R)$ enters the semiconductor, where *R* is the reflectance. In the semiconductor, light is absorbed according to the Beer-Lambert law, and the intensity of the light beam is given by $S(t, z) = S_{z0}(t)(1 - R)e^{-\alpha z}$, where α is the absorption coefficient. If we assume an homogeneous illumination onto the photoconductor of area $A = l \times w$, we have a direct relation between the time average pumping optical power P_{opt} and the time average intensity: $P_{opt} = l \times w \times S_0$. The density of electron-hole pairs created by light absorption is:

Eq. 7 $$g(z,t) = -\frac{1}{h\nu}\frac{\partial S}{\partial z} = \frac{1}{h\nu}\alpha S_{z0}(t)(1 - R)e^{-\alpha z} = \frac{1}{h\nu}\alpha(1 - R)e^{-\alpha z}S_0(1 + \cos(\omega_b t + \varphi))$$

where $h\nu$ is the energy of one photon, $\nu = \frac{\omega}{2\pi}$ being the average frequency of the laser light ($\omega \approx \omega_1 \approx \omega_2$).The electron density in the semiconductor $n(\vec{r}, t)$ can be calculated by using the continuity equation:

Eq. 8 $$\frac{\partial n(\vec{r}, t)}{\partial t} = g(\vec{r}, t) - \frac{n}{\tau} + \frac{1}{e}\nabla \vec{J}(\vec{r}, t)$$

where n/τ correspond to the recombination/trapping rate of the free carriers , with τ the carrier lifetime of the material. $\vec{J} = \vec{J}_{diff} + \vec{J}_{drift}$ is the current density, composed of diffusion and drift currents: $\vec{J}_{diff} = -eD\vec{\nabla}n$ and $\vec{J}_{drift} = -ne\vec{v} = ne\mu\vec{E}$, where $\vec{E}$ is the electric field. Here we assume that the charge neutrality is preserved everywhere in the device. The diffusion current is negligible compared to the carrier trapping due to the short life-time of the photoconductive material, in the order of $\tau \approx 1$ ps. In a standard planar photomixer, absorption of light follows the Beer-Lambert-law, and the free electron density can be approximated by $n(z) = n_0 e^{-\alpha z}$. The diffusion current becomes $J_{diff} = -\frac{D\partial^2 n}{\partial^2 z} = D\alpha^2 n$. The typical absorption coefficient in semiconductors such as LT-GaAs is $\alpha \approx 10^4$/cm. The diffusion constant is $D = k_B T\mu/e \approx 30$ cm^2 s^{-1} at room temperature, assuming a typical mobility of $\mu \approx 1000$ cm^2 V^{-1}s^{-1} in low carrier lifetime materials. The diffusion contribution to $\partial n/\partial t$ is then $D\Delta n \approx n \times 3.10^9\, s^{-1}$ and can be neglected since it is much smaller than the trapping rate $n/\tau \approx n \times 10^{12} s^{-1}$.

In the absence of currents or at small electric fields, where the contribution of the drift current J_{drift} to $\partial n/\partial t$ can be neglected, the continuity equation takes the form:

Eq. 9
$$\frac{\partial n(\vec{r},t)}{\partial t} = g(\vec{r},t) - \frac{n(\vec{r},t)}{\tau}$$

with $g(\vec{r},t) = \frac{1}{h\nu}\alpha(1-R)e^{-\alpha z}I_0(1+\cos(\omega_b t+\varphi))$ and without loss of generality we can choose the time origin such as $\phi = 0$.

The electron concentration can be then written as:

Eq. 10
$$n(z,t) = n_0(z)\left[1+\frac{\cos(\omega_b t+\psi)}{\sqrt{1+(\omega_b\tau)^2}}\right]$$

with $\psi = \text{atan}(\omega_b t)$ and $n_0(z) = \frac{\tau\alpha(1-R)e^{-\alpha z}S_0}{h\nu}$

The photogenerated charge carriers move towards the electrodes along the electric field lines. In general, the transit time τ_{tr} of a charge carrier moving from one electrode to the other depends on the position at which the latter is created due to different path lengths and field strengths. In the basic model analyzed here, we assume at low electric field E that $\tau_{tr} = l/v = l/\mu E$. The ratio of lifetime over transit time is also known as the photoconductive gain, $\gamma = \tau/\tau_{tr}$. It can be thought as the number of electrons delivered to the electrode for each electron-hole pair created.

The current generated by the photoconductor is given by the flux of charge carriers at the electrodes. For the simplest model, the current density is $j = j_c + j_d$ with $j_c = nev$ and $j_d = \varepsilon\frac{\partial E}{\partial t}$. By integration, the conduction photocurrent becomes:

Eq. 11
$$I_c(t) = \int_0^w dy\int_0^d j_c dz = evw\int_0^d n(z,t)dz = \frac{e}{h\nu}\mu E w S_0(1-R)\left(1-e^{-\alpha d}\right)\tau\left[1+\frac{\cos(\omega_b t+\psi)}{\sqrt{1+(\omega_b\tau)^2}}\right]$$

Eq. 12
$$I_c(t) = \frac{e}{h\nu}\gamma\eta_{opt}P_{opt}\left[1+\frac{\cos(\omega_b t+\psi)}{\sqrt{1+(\omega_b\tau)^2}}\right]$$

where $\eta_{opt} = (1-R)(1-e^{-\alpha d})$ is sometimes called the optical quantum efficiency and is in our case the ratio of the photon flux absorbed in the active layer to the incident photon flux. As far as concerned the displacement current, if we suppose the charge density in the semiconductor negligible in comparison with the charge density on the metallic electrodes we can consider that $E = V/l$=cste and:

Eq. 13
$$I_d(t) = \int_0^w dy\int_0^d j_d dz = \frac{dw}{l}\varepsilon\frac{dV}{dt} = C\frac{dV}{dt}$$

with *C*, the electrical capacitance of the photoconductor. In a first time, we suppose that there is only a perfect dc voltage source in parallel with the photoconductor (see Figure 2), $V = cste$ and $I_d = 0$. The photoresponse of the photomixer is defined as $\mathcal{R} = \bar{I}/P_{opt}$. From the last equation, we can notice that $\mathcal{R} \leq e/hv$. The term e/hv is approximately 1.25 A/W for a laser wavelength of 1.55 µm and 0.63 A/W at 780 nm. Photomixers at longer wavelengths can ideally be more efficient due to the higher number of photons impinging on the photomixer at the same optical power.

2.1.2 Electrical Model

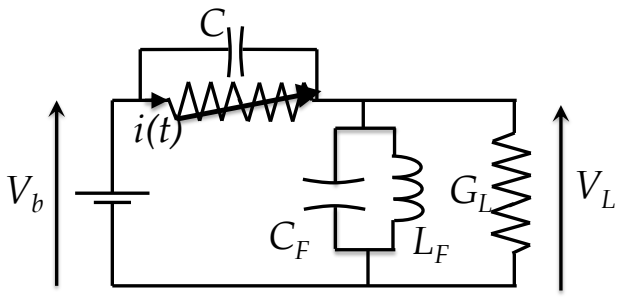

Figure 3: Electrical model of a photoconductor coupled to a load admittance G_L

The current generated by a photoconductor without a load resistance has been calculated in the previous section. However, in practice, the photoconductor can be coupled to different loads depending on the cases: to an antenna to radiate the THz currents in free space, to a waveguide followed by a powermeter or a spectrum analyser, etc. In the simplest case, the impedance seen by the photoconductor is real and is in the order of 50 ohm, as it will be seen later that the radiation resistance of broadband antennas is in the same order of magnitude as the standard impedance of microwave instruments. The THz power dissipated in the load then depends also on the capacitance of the photodetector. For the analysis of the electric circuit, it is helpful to calculate the conductance of the photoconductor:

Eq. 14

$$G(t) = \frac{I_c}{V} = \frac{e}{hvV}\frac{\tau}{\tau_{tr}}\eta_{opt}P_{opt}\left[1 + \frac{\cos(\omega_b t + \psi)}{\sqrt{1 + (\omega_b \tau)^2}}\right]$$

At low voltage, in constant mobility regime, $v = \mu E = \mu V/l$, $\tau_{tr} = \frac{l}{v} = \frac{\mu V}{l^2}$ and $\frac{\partial G}{\partial V} = 0$

In this case, *G* can be written as:

Eq. 15

$$G(t) = G_0 + G_1 \cos(\omega_b t + \psi)$$

where

Eq. 16

$$G_0 = \frac{e}{hv}\frac{\mu\tau}{l^2}\eta_{opt}P_{opt} = \frac{e\mu\overline{n_0}A}{l}$$

with $\overline{n_0}$ the spatial average value of $n_0(z)$.

Eq. 17
$$G_1 = \frac{G_0}{\sqrt{1+(\omega_b \tau)^2}}$$

To simplify the calculation, we assume that the photoconductor is coupled to a real load admittance G_L and a band pass filter consisting of an LC circuit, having a resonance frequency at ω_b, is added in parallel with the load in order to short-circuit the load at every frequency except the beating frequency (as shown in Figure 3). Voltages and currents in the circuit are time periodic (period $T=2\pi/\omega_b$). They can be expressed in Fourier series and the band pass filter removes all the upper harmonics. By using this simplification and by set $\psi = 0$ to lighten the notations, the voltage across the photoconductor takes the simple form:

Eq. 18
$$V(t) = V_{dc} + V_{ac}\cos(\omega_b t + \varphi)$$

and the current:

Eq. 19
$$I(t) = I_{dc} + I_{ac}\cos(\omega_b t + \delta)$$

It remains to calculate V_{dc}, V_{ac}, I_{dc}, I_{ac}, φ, δ. To do that, we use:

1. The relationship between the voltage and the current across the photoconductor: $I(t) = G(t)V(t)$ where we use the complex notation, i.e. $I_{ac}\cos(\omega_b t + \delta) = Re(i_{ac}(\omega_b)e^{j\omega_b t})$, $V_{ac}\cos(\omega_b t + \delta) = Re(v_{ac}(\omega_b)e^{j\omega_b t})$, etc.

we find from this latter:

Eq. 20
$$I_{dc} = V_{dc}G_0 + \frac{1}{2}V_{ac}G_1\cos\varphi \qquad i_{ac} = G_0 v_{ac} + G_1 V_{dc}$$

2. The Kirchhoff's current law at $\omega = \omega_b$ which gives (see Figure 4a): $-G_L V = I + C\frac{dV}{dt}$ which can be expressed in complex notation by:

Eq. 21
$$-G_L v_{ac} = i_{ac} + jC\omega_b v_{ac}$$

Thereby, V_{ac} and φ can be calculated:

Eq. 22
$$V_{\mathrm{ac}} = V_{\mathrm{dc}}\frac{G_1}{\sqrt{(G_0+G_L)^2 + C^2\omega_b^2}} \text{ and } \varphi = \pi - \operatorname{atan}\left(\frac{C\omega_b}{G_0+G_L}\right)$$

In addition, the band-pass filter short-circuits G_L at $\omega = 0$ and then: $V_{dc} = V_b$. (see Figure 4b)

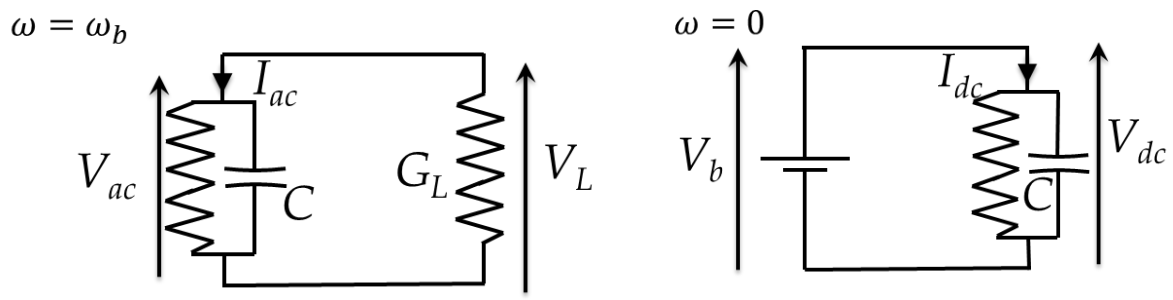

Figure 4: a) Electrical circuit at $\omega = \omega_b$ and b) $\omega = 0$

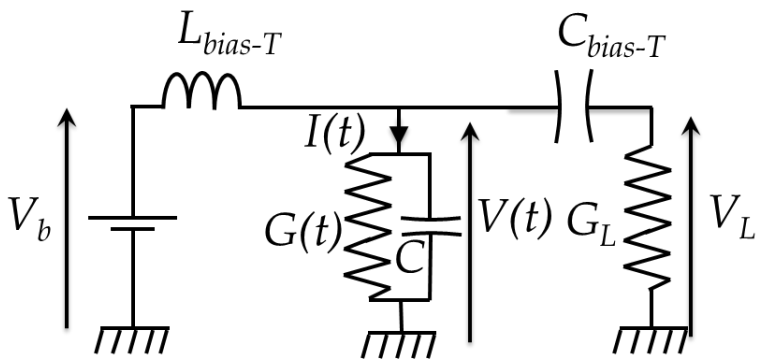

Figure 5: Photomixing experiment AC/DC decoupling using a Bias-T

The LC circuit filters all the frequencies except for $\omega = \omega_b$. It is obvious that this is a calculation "trick" to obtain easily the voltage and current in the circuit, which is very difficult to use in practice since it limits dramatically the frequency band of the photomixing source. In practice, there is always a circuit which decouples dc and ac parts of the generated currents in the circuits. It is done straight when an antenna is used to radiate the ac currents in free space. A bias-T is inserted, when waveguide measurements are performed (see Figure 5), resulting in the same ac/dc decoupling but without cancelling the signals at harmonics frequencies ($2\omega_b, 3\omega_b,$ etc.). The theoretical results obtained here can thus be used also in this case but only when the higher harmonics are negligible (which is often true…). From the equations above, we can deduce directly the small signal equivalent circuit at $\omega = \omega_b$ which consists of a current source $I_{ac} = |i_{ac}| = G_1 V_b$ having an internal conductance G_0 in parallel with the electrical capacitance of the photodetector and loaded by a conductance G_L (see Figure 6).

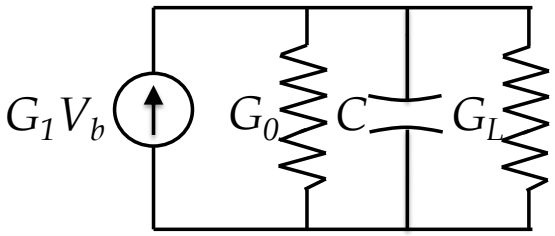

Figure 6: Small signal Equivalent circuit at ω_b

2.1.3 Efficiency and Maximum power

2.1.3.1 (1) Case G_1=G_0 and C=0

It is rather obvious that the electrical capacitance of the photoconductor limits the performance at very high frequencies. It is however interesting to deal with the ideal case where $C\omega_b \ll (G_0 + G_L)$

From the calculations above, the power provided by the dc generator is:

Eq. 23
$$P_{dc} = I_{dc}V_b = V_b^2\left(G_0 - \frac{1}{2}\frac{G_1^2}{G_0 + G_L}\right)$$

The average RF power dissipated in the load G_L is:

Eq. 24
$$P_{THz} = \frac{1}{2}G_L V_1^2 = \frac{1}{2}V_b^2\frac{G_L G_1^2}{(G_0 + G_L)^2} = \frac{1}{2}V_b^2\frac{G_L G_1^2}{(G_0 + G_L)^2} = \frac{1}{2}I_{ac}^2\frac{G_L}{(G_0 + G_L)^2}$$

The maximum power dissipated in the load is obtained at the impedance matching condition when $G_0 = G_L$. It is also known as the "maximum available power" of a source by microwave engineers. In the most favorable case, when the carrier lifetime is much smaller than the beating period $G_0 \approx G_1$, it can be written as:

Eq. 25
$$P_{\max} = \frac{1}{8}G_0 V_b^2$$

The conversion efficiency is then (when $G_0 \approx G_1$) equal to:

Eq. 26
$$\eta_{G_L=G_0} = \frac{P_{max}}{P_{dc}} \approx 0.167$$

It is worth noting that it doesn't correspond exactly to the maximum efficiency which is reached when $G_L = \frac{G_0}{\sqrt{2}}$:

Eq. 27
$$\eta_{\max} = \frac{1}{(\sqrt{2}+1)^2} \approx 0.172$$

2.1.3.2 General Case

We consider here the more general case where the electrical capacitance is not negligible and the load admittance is not a pure conductance and has the form $Y_L = G_L + jB_L$. The dissipated power in Y_L is now:

Eq. 28
$$P_{THz} = \frac{1}{2}I_{ac}^2\frac{G_L}{(G_0 + G_L)^2 + (\omega_b C + B_L)^2}$$

which takes the form when the expression of G_1 and I_{ac} are put in Eq. 28.

Eq. 29
$$P_{THz} = \frac{V_b^2 G_0^2}{2}\frac{G_L}{[(G_0 + G_L)^2 + (\omega_b C + B_L)^2](1 + \omega_b^2\tau^2)}$$

The maximum power dissipated in the load is obtained when $Y_L{}^* = Y_S$, i.e. when $G_0 = G_L$ and $B_L = -C\omega_b$ and is equal to the previous case. If the load is a pure conductance ($B_L = 0$) and if $G_L \gg G_0$, Eq. 29 takes the form popularized by E. Brown and coworkers [8]:

Eq. 30
$$P_{THz} = \frac{I_{dc}^2}{2}\frac{R_L}{[(1 + (\omega_b R_L C)^2](1 + \omega_b^2\tau^2)}$$

Here, we have defined $R_L = 1/G_L$. It can be noted that $I_{dc} = \mathcal{R} \cdot P_{opt}$. We recognized the two cut-off frequencies related to the RC time constant (f_{RC}) and to the carrier lifetime in the photoconductive material (f_τ) .

2.2 Photodiode

2.2.1 PIN photodiodes

As previously mentioned, another kind of semiconductor device that can be used as photomixer is the pn junction photodiode. Electrons are holes photogenerated in the depletion region of a pn junction are accelerated towards the electrodes by the built-in potential, giving rise to a photocurrent. However, p-n homojunctions with constant doping in the p and n regions are not very efficient photodiodes. At high doping concentrations, the depletion region in which carrier transport is efficient (drift) becomes narrow, and only a small portion of the incoming light can be absorbed in or close to the depletion region. Lower doping concentrations increase the depletion region width, but also make the formation of low resistance ohmic contacts more difficult.

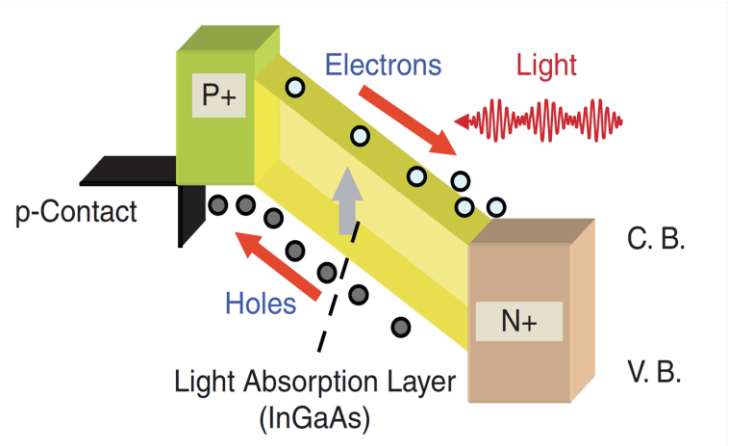

Figure 7 : Schematic band diagram of a p-i-n photodiode (from [13])

The main problems of p-n junctions for photodetectors can be overcome by adding an intrinsic layer between the p and n regions. A schematic band diagram of such a p-i-n diode is shown in Figure 7. P-i-n diodes allow high doping concentrations for low resistance ohmic contacts, independent from the width *w* of the intrinsic layer. This latter is an important design parameter: it should be large enough to absorb most of the impinging radiation and to reduce the capacitance of the device, but it should be as small as possible to reduce the transit time of the charge carriers. Minority carriers that are generated in the doped regions are subject to diffusion. Only after diffusing into the intrinsic region, they are accelerated efficiently by the electric field. The doped regions of p-i-n diodes are therefore often fabricated from a material with larger bandgap than the photon energy at the operation wavelength. Light absorption and photogeneration of charge carriers then only takes place in the intrinsic region, where the charge carriers are separated efficiently by the electric field. The frequency response of p-i-n diodes has a RC-roll-off in a similar manner to that of photoconductors. Recombination of photogenerated charge carriers is negligible, and the transit time determines the frequency response instead of carrier the lifetime as in the case of the photoconductors. The p-i-n

photodiodes are not suited for THz photomixing because the low drift velocity of holes in most of the III-V semiconductors materials results in an intrinsic low frequency bandwidth and a low saturation current because of the space charge accumulation in the intrinsic layer screening the bias field.

2.2.2 Uni-Traveling-Carrier Photodiodes

Uni-Travelling-Carrier Photodiodes (UTC-PD) have been proposed in 1997 by researchers of the NTT laboratory [14][15] in order to overcome the limitations of the InP/InGaAs p-i-n photodiodes in terms of frequency response and photocurrent saturation. As seen in Figure 8, UTC-PD's have a p-i-n diode-like structure in which the absorption of light and the carrier collection are achieved in two disjoint regions. The GaInAs absorption layer is heavily p-doped leading to a frequency response which is not limited anymore by the transit time of low-saturation velocity holes in GaInAs (v_h=5×10^6 cm/s) but by the electron motion in the InGaAs absorption and InP collection layer (v_e=4×10^7 cm/s in InP). The hole response time is indeed very fast since it is related to the dielectric relaxation time $\tau_R = \varepsilon/\sigma = \varepsilon/e\mu_h p_0$ where p_0.is the doping concentration. For example, if $p_0 = 1 \cdot 10^{18}$ cm^{-3}, $1/(2\pi\tau_R) \approx 30$ THz. Thanks to a blocking layer, electrons only diffuse/drift towards the InP collection layer, which they drift across at their overshoot drift velocity. Furthermore, the photocurrent saturation level is improved because of the reduction of the space charge effect in the collection layer induced mainly by the slow holes in the pin photodiodes.

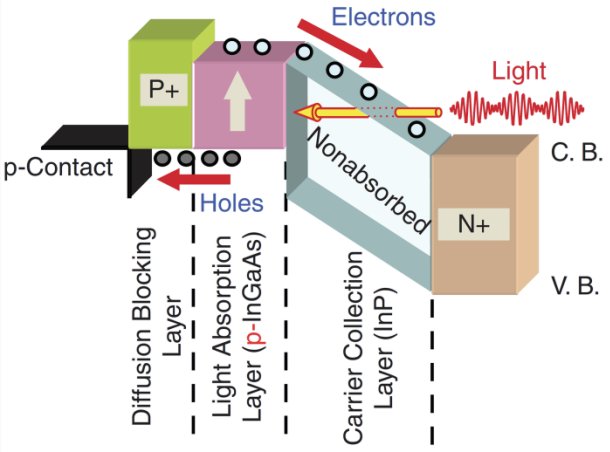

Figure 8 : Schematic band diagram of a UTC photodiode (from [13])

2.2.3 Photocurrent generation

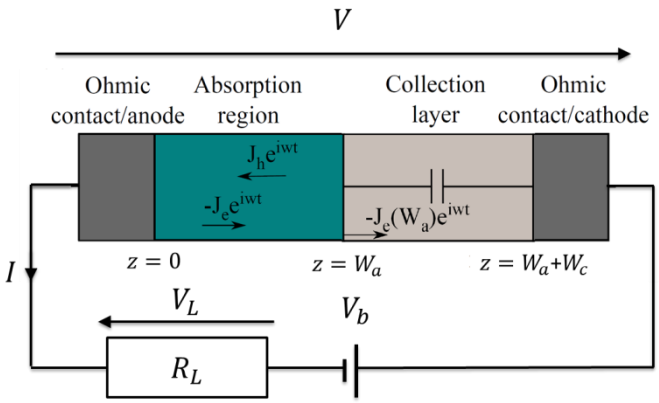

Figure 9 : Electric model of a UTC photodiode (derived from[16])

In order to model the photocurrent generation in an UTC photodiode, we use the works of Ishibashi et al.[16] and M. Feiginov[17] and we assume, as previously, an homogeneous illumination onto a diode of area A.The current density flowing through the device consists of the sum of electron and holes conduction current densities and of the displacement current. Since it is constant along the device, it is equal to its average on the diode thickness (see Figure 9):

Eq. 31
$$I(t) = \frac{A}{W}\int_0^W (J_e(t) + J_h(t) + \varepsilon\frac{\partial E}{\partial t})\,dz$$

In a photomixing experiment, as already seen the current in the device consists of a dc part and an alternating component at the beating frequencyω: $I(t) = I_{dc} + I_{ac}\cos(\omega t + \phi)$. In the following we are interested only in the oscillating component and we use the complex notation where $I_{ac}\cos(\omega t + \phi) = Re(i_{ac}(\omega)e^{j\omega t})$.

Eq. 31 takes thus the form:

Eq. 32
$$i_{ac}(\omega) = \frac{A}{W}\int_0^W (j_e(\omega) + j_h(\omega) + j\omega\varepsilon E)\,dz$$

And the Kirchhoff's voltage law for the oscillating terms (since $V_b = cste$) gives:

Eq. 33
$$0 = v_{ac} + R_L i_{ac}$$

where $v_{ac} = \int_0^W E\,dz$. By injecting Eq. 33 in Eq. 32, we obtain:

Eq. 34
$$i_{ac}(\omega) = \frac{i_c(\omega)}{1 + j\omega R_L C}$$

with

Eq. 35
$$i_c(\omega) = \frac{A}{W}\int_0^W (j_e(\omega) + j_h(\omega))\,dz$$

with $C = \varepsilon A/W$, the electrical capacitance of the device. As a matter of fact, it can be shown that this capacitance is composed of the p-doped absorption layer capacitance in series with the nid InP collector layer $\frac{1}{C} = \frac{1}{C_a} + \frac{1}{C_c}$ with $C_a \gg C_c$, that is why we will consider from now that:

Eq. 36
$$C \approx \varepsilon A/W_c$$

$i_c(\omega)$ can be divided in two parts:

Eq. 37
$$\frac{A}{W}\int_0^W (j_e(\omega) + j_h(\omega))\, dz = \frac{A}{W}\int_0^{W_a} (j_e(\omega) + j_h(\omega))\, dz + \frac{A}{W}\int_{W_a}^W j_e(\omega)\, dz$$

The hole current in the collector is neglected since the holes are blocked by the potential barrier at the interface between the absorption layer and the collector layer. The current densities are calculated in the drift diffusion approximation by using the poisson equation and the continuity equations in 1D:

Eq. 38
$$\frac{\partial n}{\partial t} = g - \frac{n}{\tau} + \frac{1}{e}\frac{\partial j_e}{\partial z} = g - \frac{n}{\tau} - \frac{\partial}{\partial z}\left(\mu_e n(E_0 + E) - D_e \frac{\partial n}{\partial z}\right)$$

Eq. 39
$$\frac{\partial p}{\partial t} = g - \frac{p}{\tau} - \frac{1}{e}\frac{\partial j_h}{\partial z} = g - \frac{p}{\tau} - \frac{\partial}{\partial z}\left(\mu_h (p + p_0)E - D_h \frac{\partial p}{\partial z}\right)$$

where p and n are the photogenerated charge carriers, $p_0$is the background hole density in the absorption layer, g is the carrier generation rate (see previous section related to photoconductor) and τ is the recombination lifetime in the absorption layer, E is the electric field induced by the photogenerated carriers. E_0 is a quasi field acting on the electrons in the absorption layer, which can be added by a proper design of the epitaxial layer stack in order to shorten the diffusion time of the electron out of this latter.

It can be shown according to this model[16] and by neglecting the contact resistances that:

Eq. 40
$$i_c(\omega) = -\frac{e}{hv} P_{opt}(1 - e^{-\frac{W_a}{\delta}}) \frac{1}{1 + j\omega\tau_a} \frac{\sin(\frac{\omega\tau_{tr}}{2})}{\frac{\omega\tau_{tr}}{2}} e^{-j\frac{\omega\tau_{tr}}{2}}$$

Where P_{opt} is average optical power illuminating the UTC photodiode. In this model we neglect the reflections and losses in the structure. $\delta = \frac{1}{\alpha}$ is the absorption depth in the InGaAs layer.

Without a quasi-field in the absorption layer, the electron dynamics is related to diffusion. In that case:

Eq. 41
$$\tau_a \approx \frac{W_A}{v_{th}} + \frac{W_A^2}{2D_e}$$

with v_{th} is the thermionic emission velocity, approximately equal to $v_{th} \approx 1 \cdot 10^7 cm/s$ in $In_{0.53}Ga_{0.47}As$ [16], [17]. For a reasonable absorption layer thickness of around 150 nm and assuming a mobility $\mu_e \approx 5000\ \mathrm{cm^2 V^{-1} s^{-1}}$, it gives $\tau_a \approx 2.3\ ps$ and response speed is limited by the electron diffusion wiith a 3dB cutoff frequency of 67 GHz. A quasi field in the absorption layer increases the frequency response by adding a drift to the electron diffusion. It is included during the epitaxial

growth either by a composition gradient or a doping gradient of the InGaAs layer. It has been shown [17] that when the drift velocity $v_d > v_{th}$ the diffusion related time constant can be approximated by $\tau_a \approx \frac{W_A}{v_d}$.[17]. The drift velocity can exceed $2 \cdot 10^7$ cm/s, in which case the 3dB cutoff frequency is increased to 200 GHz for the same 150-nm-thick absorption region. The faster electron transport in the absorption layer due to the built-in quasi-field is also important to reduce the carrier density and improve the response of the device in the high injection regime[18]. The electron transit time across the collector layer is given by τ_{tr}. An advantage of the UTC diodes over p-i-n diodes is that only electrons flow across this layer and therefore by $\tau_{tr} \approx \frac{W_C}{v_d}$ is shorter than for these latter at identical layer thickness. Moreover, electrons reach their saturation velocity at relatively low electric field strengths (<100 kV/cm) because of their high mobility. A reverse bias in the order of -1 V is sufficient for efficient operation of UTC photodiodes with ~100 nm thick collector layers. In addition, it is worth noting that velocity overshoot could play an important role in the collector layer, further decreasing τ_{tr}. The overshoot electron velocity in InP can reach $4 \cdot 10^7 \mathrm{cm/s}$[18]. In this case, the 3dB frequency related to τ_{tr} is around 900 GHz for a 200-nm-thick collector layer which is clearly well beyond the cutoff frequency related to the diffusion time τ_a.

2.2.4 Electrical Model and Output power

We can note from Eq. 40 that, in this model, the photocurrent doesn't depend on the voltage, in other words, the internal photoconductance of the photodiode is zero (i.e. $G = \frac{\partial I}{\partial V} = 0$). The equivalent electrical circuit of the photodiode is thus only an AC photocurrent source ($i_c(\omega)$ defined in Eq. 40) in parallel with a capacitance C. Obviously, in a full model of the frequency response of the photodiode, there is a small internal conductance since it is well known[19] that at high photocurrent, the frequency response of the photodiode was improved by adding an external bias voltage in order to balance the space charge screening in the device. In addition, it is clear that in a full model, the contact resistance should be added.

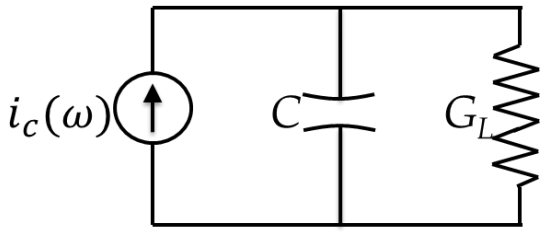

Figure 10: Equivalent circuit of an UTC photodiode at ω ($G_L = 1/R_L$)

Concerning the power dissipated in load of admittance $Y_L = G_L + jB_L$, we can take the expression obtained in the case of a photoconductor with $G_0 = 0$. We obtain:

Eq. 42

$$P_L = \frac{1}{2}\frac{\left|i_c\right|^2 G_L}{(G_L)^2 + (\omega C + B_L)^2}$$

which becomes when $B_L = 0$ and if we use the expression of i_c:

Eq. 43

$$P_L = \frac{1}{2} R_L i_{dc}^2 \frac{1}{1+(\omega R_L C)^2} \frac{1}{1+(\omega \tau_a)^2} \left| \frac{\sin(\frac{\omega \tau_{tr}}{2})}{\frac{\omega \tau_{tr}}{2}} \right|^2$$

where $i_{dc} = -\frac{e}{hv} P_{opt}(1 - e^{-\frac{W_a}{\delta}})$.

It is worth noting we have here three time constants instead of only two in the case of ultrafast photoconductors which can explain the highest power measured with LT-GaAs photomixers in comparison with UTC photodiodes at frequency above 2 THz (see for example [20]).

2.3 Frequency down-conversion using photomixers

The demonstration of homodyne (or heterodyne) detection with identical photomixers performed by S. Verghese and coworkers [21] paved the way to practical photomixing systems by avoiding helium cooled bolometer detection. However the photomixer used as detector have attracted little attention, although the requirements are quite different. First of all, as detectors, the photoconductor is biased only by the terahertz field which lies typically in the mV range. Therefore high breakdown voltage is not required. In counterpart, high low field mobility is a mandatory feature. As for the emitter, a low photocarrier lifetime and low electrical capacitance will fixed the high frequency performances. In addition of a high sensitivity, a low dark current, obtained with a high resistivity photoconductive material, minimizes the Johnson noise even if the noise floor is mainly due to the shot noise, as it has been shown in time-domain spectroscopy systems [22]. With regards to 0.8-µm-laser systems, only few improvement has been achieved since the development of the standard planar photoconductor on LT-GaAs [23]. Homodyne detection systems have been also reported using alternative photoconductive material, such as ion implanted GaAs [24] with no improvement until the development of optical cavity LT-GaAs photoconductors that we will present in the following part[25]. Things are very different with respect to the 1.5-µm-wavelength laser systems. The development of highly sensitive, high-dark-resistivity photoconductors working at this pump wavelength is a very challenging task which opens the way to low-cost and highly reliable systems thanks to the availability of standard telecom-fiber components. Photodiodes are efficient emitters but poor detectors as we will see below. Their built in internal electric field indeed results in a photoresponse depending slightly of the applied bias voltage unlike the photoconductors even if nonlinear effects are still possible allowing down conversion with low efficiency[26][27]. Photoconductive materials developed for THz generation with 1.5-µm-wavelength lasers, such as high energy ion implanted InGaAs[28], Fe:InGaAs[29], Rd:InGaAs[30] or beryllium doped low

temperature grown InGaAs present a carrier life time reaching the sub-picosecond range, close to the values of the LT-GaAs but exhibit low dark resistivity (~1 KΩ.cm), increasing the Johnson noise and thus increasing the noise equivalent power of the detector. The best results have been obtained with a 2-µm-thick multi nanolayer stack of low Beryllium doped LT-InGaAs absorbing layer, presenting a low carrier lifetime and InAlAs layer used as electron trapping layers to increase the dark resistivity of the LT-InGaAs layers[31][32].

2.3.1 Electrical model: conversion loss

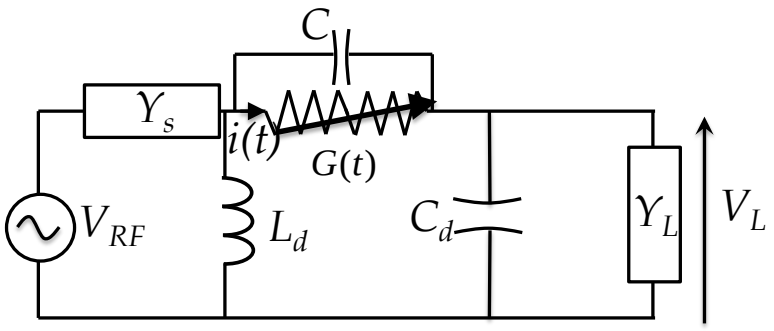

Figure 11: Heterodyne mixing in a photoconductor illuminated by an optical beatnote

In the general case of heterodyne detection by means of a photoconductor pumped by a beating note of two lasers beams, the dc voltage source is replaced by a RF/THz wave of frequency f which will be down-converted to an intermediate frequency f_{IF} such as $f_{IF} \ll f_{RF}$. The beatnote frequency f_b is then chosen such as $|f_{RF} - f_{IF}| = f_b$. Once again, the wide tunability provided by the use of a laser beatnote give the possibility to obtain a wideband heterodyne receiver only limited by the frequency response of the photoconductor. The main figure of merit of a heterodyne mixer is the conversion loss between the power of the incident THz wave (P_{THz}) and that of the down-converted signal(P_{IF}) :

Eq. 44

$$L = \frac{P_{THz}}{P_{IF}}$$

In Figure 10 is shown the equivalent electrical circuit in which the photoconductance biased by the incident THz wave modeled by an alternating source of internal admittance Y_s and electromotive force:

$$V_{THz}\cos(\omega_{THz}t)$$

In addition, it is assumed that the IF signal is filtered on the THz side by a coil of inductance L_d and the THz waves are filtered on the IF side by a capacitor of capacitance C_d, chosen to obtain a short-circuit at ω_{THz} and an open circuit at ω_{IF}. Conversely, L_d is chosen such that an open circuit at ω_{THz} and a

short-circuit at ω_{IF} are obtained. Furthermore, as previously mentioned, the phoconductor illuminated by the optical beatnote is modeled by a time dependent photoconductance:

$$G(t) = G_0 + G_1 \cos(\omega_b t)$$

By neglecting the harmonics generated in the circuits, the current and the voltage across the photoconductor have the following form:

$$V(t) = V_0 \cos(\omega_{THz} + \phi) + V_{IF} \cos(\omega_{IF} t + \delta)$$

$$i(t) = i_0 \cos(\omega_{THz} + \phi_i) + i_{IF} \cos(\omega_{IF} t + \delta_i)$$

with $\omega_{IF} = |\omega_{THz} - \omega_b|$

By using again the relation $i(t) = G(t)V(t)$, the Kirchhoff laws at both frequencies (ω_{THz} and ω_{THz}) and by assuming that $V_{IF} \ll V_{THz}$, it is found in the simplest case where $Y_s = Y_L$ and $C = 0$[25]:

Eq. 45

$$L = \frac{(G_0 Z_s + 1)^4}{G_1^{\,2} Z_s^2}$$

In the ideal case $G_1 = G_0$ and *L* has a minimum L_{min}=16 when $Ys = Y_L = G_0$

It gives in dB, $L_{dB} = 12\,\mathrm{dB}$

We have shown once again that the photoconductance G_0 must have a value close to that of load admittance or internal admittance of the THz source to reach the minimum conversion loss. The values obtained are in that case comparable to those of electronics mixers based on Schottky diodes.

3 Standard Photomixing devices

3.1 Planar photoconductors

Following the first demonstration of THz generation by photomixing by E.R Brown *et al.* [8], ultrafast photoconductors used for the generation of THz waves by photomixing have been designed on the model of the metal-semiconductor-metal photoconductors using interdigitated metallic electrodes patterned on a subpicosecond-carrier-lifetime photoconductive material. This first demonstration has been performed by using an LT-GaAs layer compatible with 800-nm-wavelength light but since then, various ultrafast photoconductive materials working at 800 nm or 1550 nm have been tested with always the same electrodes topology[20], [33]–[37]. It is shown in Figure 12 a SEM picture of this standard topology. It consists of five 200-nm-wide and 6-µm-long contact electrodes spaced from 1.8 µm apart. The active area of the photoconductor is 64 µm².

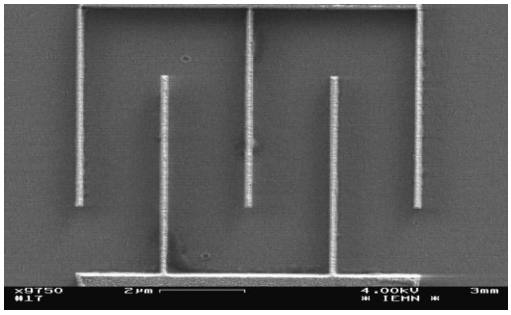

Figure 12: SEM picture of an ultrafast photoconductor based on interdigitated electrodes patterned on a low-carrier lifetime photoconductive material.

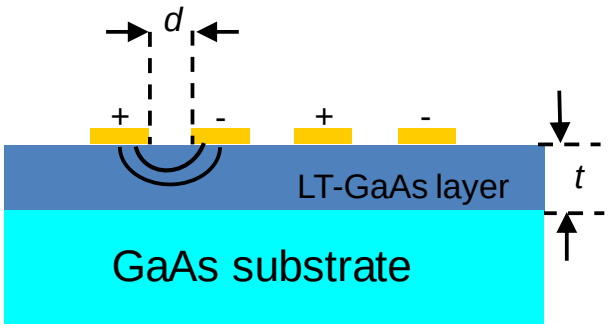

Figure 13: LT-GaAs planar photoconductor

A THz bandwidth is obtained by using a sub-picosecond lifetime material such as LT-GaAs, LT-InGaAs, InGaAs:Fe, etc. and by limiting the electrical capacitance of the set of interdigitated electrodes at values in the order of few femtofarads. Moreover, the photodetector size should be lower than ten microns in order to attenuate the effects due to wave interferences occurring when the electromagnetic waves wavelength is comparable with the dimensions of the device. The load impedance (antenna radiation impedance, waveguide characteristic impedance, powermeter impedance, etc.) is in the range of 50 to 100 Ohms, the $R_L C$ time constant is then also sub-picosecond. To be more specific, the planar photodetectors based on LT-GaAs shown in Figure 12 and Figure 13 have the properties below:

- ✓ $200\ \text{fs} < \tau < 1\ \text{ps} \rightarrow 160\ \text{GHz} < f_\tau < 800\ \text{GHz}$
- ✓ $0.5\ \text{fF} < C < 3\ \text{fF}$ and $R_L \approx 50\ \text{Ohm} \rightarrow 25\ \text{fs} < R_L C < 150\ \text{fs}$ and $6\ \text{THz} > f_{R_L C} > 1\ \text{THz}$
- ✓ $d \approx 2\ \mu\text{m} \rightarrow$ Photoresponse $R \approx 4 \cdot 10^{-2}\ \text{A/W}$ with an antireflection coating and $t \approx 2\ \mu\text{m}$ (see further for the justification of the need of $t \approx d$)
- ✓ $P_{opt} \approx 100\ \text{mW}\ \mu\text{m}$ at thermal failure, $I_{dc} \approx 2\ \text{mA}$ and $V_b \approx 20\ \text{V}$
- ✓ $G_0 \approx 10\ \text{k}\Omega$

By using Eq. 30 with these values, we obtain an output power of $P \approx 10\ \mu W$ at 300 GHz and $P \approx 1\ \mu W$ at 1 THz.

3.1.1 Intrinsic limitation

As a matter of fact, the powers emitted by the planar photomixers hardly reach 10 µW at 300 GHz and 1 µW at 1 THz [33]–[37], which is still largely insufficient. In fact, the only broadband detectors sensitive enough to detect this power level with a good signal-to-noise ratio (> 1000) are the bolometric detectors operating at 4 K. The THz power is indeed limited by thermal effects [38]. For a given dc bias voltage, when the optical power is gradually increased, thermal failure occurs before saturation effects are observed in the THz power or dc photocurrent. Increasing the THz power can only be achieved by optimizing:

1 : The ratio between the power emitted and the thermal power generated in the photodetector: i.e. the electrical and optical efficiency. This amounts to increasing the photoconductor Photoresponse ($\mathcal{R}$) or the ratio G_0/P_{opt} so that the photoconductance is closer to $G_0 = 1/50\ \Omega^{-1}$.

2 : The thermal power management in close proximity of the device to hamper the temperature rise during operation

At low electric field, when the carrier mobility is constant, it has already been shown (Eq. 16) that: $G_0/P_{opt} \propto 1/l^2$ (with l the inter-electrode spacing). Furthermore, when the saturation velocity is reached at higher electric field, it is easily deduced from Eq. 11 that the maximum photoresponse ($\mathcal{R}_m$) is proportional to $1/l$. **The inter-electrode spacing should be decreased in order to increase G_0/P_{opt} and $\mathcal{R}_m$.**

We have also to take care of the thermal properties of the device. The total thermal resistance R_{th} between the photoconductor and the substrate (assumed to be at the thermal mass) can be seen as the sum of two thermal resistances in series ($R_{th1} + R_{th2}$), with R_{th1}, the contribution of the photoconductive active layer and R_{th2} the contribution of the substrate . Once again the planar structure is penalized by the thickness of the low carrier lifetime photoconductive material required ($t \approx 2\ \mu m$) .The latter has indeed a low thermal conductivity because of the high defects density (i.e. 20 $Wm^{-1}K^{-1}$ for LT GaAs, half as much as standard GaAs [39], and only 5 $Wm^{-1}K^{-1}$ for standard $In_{0.53}Ga_{0.47}As$) required to obtain a sub-picosecond lifetime. One should therefore reduce its thickness (t) to decrease R_{th}. On the other hand, the thermal conductivity of the standard growth substrate (InP or GaAs) are relatively low (55 $Wm^{-1}K^{-1}$ for GaAs, 68 $Wm^{-1}K^{-1}$ for InP), so it would seem wise to replace the semi-insulating growth substrate with a better thermal conductivity. **It is therefore necessary to reduce the inter-electrode spacing (l) and the thickness of the ultrafast photoconductive material (t).**

In the case of a planar photodetector, t and l depend on the optical absorption depth ($\delta_\alpha = 1/\alpha$) in the photoconductive material which is around 1 µm (0.7 µm at λ = 780 nm in GaAs, 1 µm at λ = 1550 nm in $In_{0.53}Ga_{0.47}As$)

1. Thus $t \approx 2\ \mu m$ is needed to optimize the optical quantum efficiency but also and especially to limit the absorption in the growth substrate in which the carrier lifetime is greater than that in the ultrafast photoconductive material by many orders of magnitude.
2. $l \approx 2\ \mu m$ is required so that the static electric field magnitude is sufficient in the whole absorption zone. Indeed, on a planar photodetector, the application of an electrical potential difference between two conductive electrodes deposited on the surface of a semiconductor considered as a dielectric produces a non-negligible static electric field down to a depth almost equal to the inter-electrode spacing. So, to have a significant electric field to a depth of 2 microns, the inter-electrode spacing must be close to this value. We will see in the next parts how this intrinsic limitation can be overcome by the use of optical cavities.

3.2 UTC Photodiodes

3.2.1 Backside illuminated UTC photodiodes

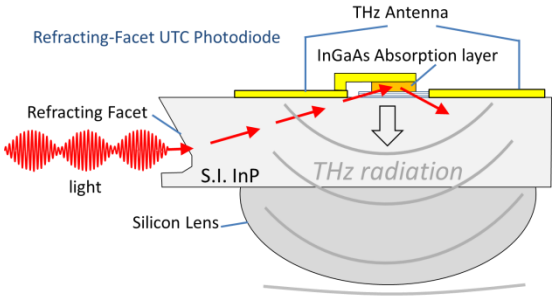

Figure 14: Refracting facet UTC photodiode (based on [13])

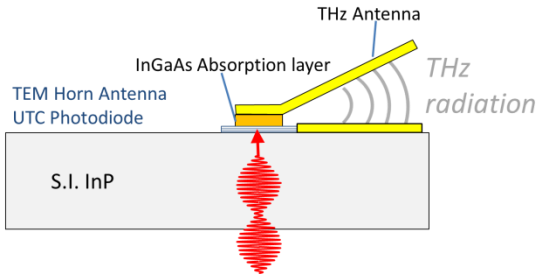

Figure 15: TEM Horn UTC Photodiode

The experimental demonstration of a cut-off frequency reaching 300 GHz [39] and a power of 20 mW generated by photomixing at 100 GHz [40] with a photocurrent reaching 25 mA has shown the potential of the uni-travelling carrier photodiode, initially developed for telecom applications, as THz photomixer. One of the main differences between both applications comes from the need of a THz antenna to radiate in free space the THz photocurrents generated in the device. As it will be seen in a next section,THz antennas monolithically integrated with photomixers are planar antennas coupled to a silicon lens which is required to obtain an efficient extraction outside the semiconductor substrate. Below 1 THz, amongst the most powerful photomixers are based on backside vertically illuminated UTC-PD. This structure use a metallic opaque top p-contact electrode essential to get good thermal properties and a low contact resistance. The backside illumination is not possible when a silicon lens is added at the backside of the substrate. As shown in Figure 14, one possibility consists

in the use of a refracting facet etched in the InP substrate used for epitaxial growth. Around 1 THz, a power of 2.6 µW has been measured when integrated with a log-periodic antenna [12] and 10.9 µW with a double-dipole resonant antenna [41]. Three-dimensional-shaped THz antennas have also been proposed to remove the need for a silicon lens. By using a TEM horn antenna monolithically integrated to a UTC photodiode illuminated through the InP substrate (see Figure 15), a power of 1.1 µW at 1 THz has been measured[42]. At lower frequencies, the waveguide-integrated photomixers associated to a matching circuit give the best results. For example, up to 0.5 mW at 350 GHz have been obtained when an UTC PD is integrated in J-Band module [43].

3.2.2 Waveguide-fed UTC photodiodes

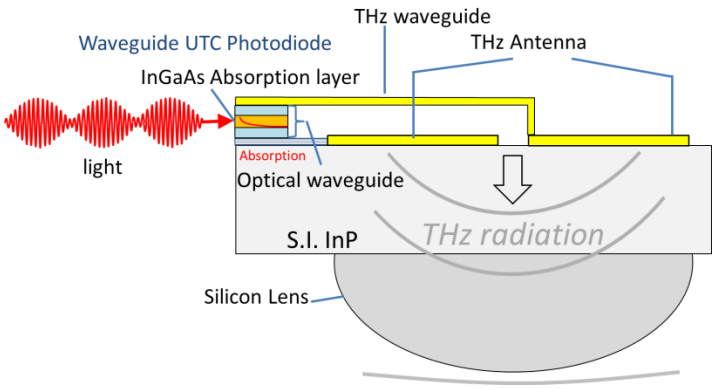

Figure 16: Waveguide UTC photodiode coupled to a planar antenna

Nevertheless, the high cut-off frequencies of the vertically illuminated UTC-PD are achieved by lowering the thickness of the absorption layer, but at the price of a low quantum efficiency and photoresponse ($\mathcal{R} < 100$ mA/W). Using the solutions already developed for p-i-n PD, edge-coupled UTC-PD have been proposed to enhance photoresponse while maintaining a high frequency bandwidth and a high photocurrent saturation. For example, a waveguide-fed UTC-PD (WG-UTC-PD) is a promising structure to achieve higher output powers (see Figure 16). This structure is illuminated by coupling the light into the facet of a semiconductor optical waveguide obtained by thinning and cleaving the InP substrate. At 200 GHz, a maximum output power of 1 mW at a dc photocurrent of 23 mA has been measured with a WG-UTC-PD integrated to a coplanar waveguide and mounted on a Peltier cooler [44]. The integration with a silicon lensed planar antenna is somewhat easier to make than in the case of the backside illumination even if there some difficulties arises because the active device is positioned at the edge of the chip. For example an additional waveguide can be needed to feed the wideband antenna at its center. These structures integrated with a resonant antenna (dipole) have delivered 124 µW at 457 GHz and 24 µW at 914 GHz [45]. However, better results, i.e. 10 µW at 1 THz at a photocurrent of 12 mA ($\mathcal{R}$ =310 mA/W), have been achieved with an edge-coupled composite p-i-n photodiode (C-PIN) integrated with a broadband antenna [46]. A C-PIN PD is

a quasi-unipolar travelling carrier photodiode. The GaInAs layer is indeed not heavily p-doped on its whole thickness. This supplementary parameter allows to both balance and reduce the response time of electrons and holes [47].

4 Optical cavity based photomixers

4.1 LT-GaAs Photoconductors

We have seen that the two main geometrical parameters of a fast photodetector, namely the thickness of the photoconductive layer (t) and the inter-electrode spacing (d) are fixed by the optical absorption depth in the photoconductive material to about 2 µm. Such a limitation can be overcome by using an optical cavity. This is not a new idea in order to improve the photoresponse of infrared photodiodes (see for example refs [48],[49],[50]). We proposed some years ago to apply this concept to ultrafast photoconductors [51], [52] by using a buried metal layer as optical reflector. This metallic reflector is more suited to the development of powerful photomixers in comparison with a bragg reflector because of its better thermal properties.

4.1.1 Optical modeling

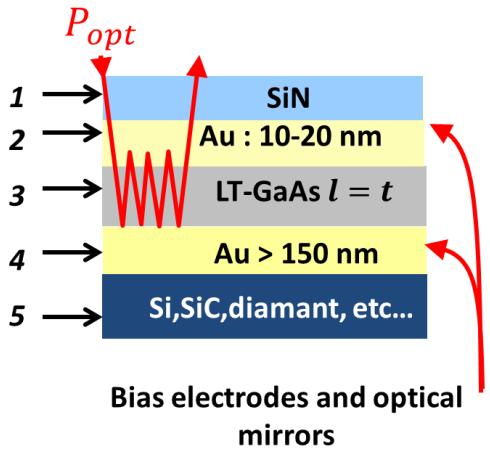

Figure 17: LT GaAs Optical cavity photoconductor

. In this structure (see Figure 17), the LT-GaAs layer (3) (or another semi-insulating photoconductor), is sandwiched between two noble metal layers (2 and 4) with low infrared loss, such as gold, silver or copper. These two metal layers have a dual role. They serve at the same time as bias electrodes of the photoconductor and as optical mirror of the optical cavity. The bottom layer (4) acts as a near-perfect metal mirror and the top layer (2) is semi-transparent and is used to tune the transmission of

the optical power in the cavity. The thickness of the layer (t) and the inter-electrode spacing (d) are now combined and can be chosen such that $t = d < \delta_\alpha$.Indeed, it is possible by using an optical Fabry-Pérot resonance, to obtain an optical quantum efficiency close to unity despite a submicron layer thickness. An infrared transparent dielectric layer (1) may be added at the surface to encapsulate the component and/or adjust the properties of the resonant cavity. This layer can consist of silicon nitride (Si_3N_4) but also silicon oxide (SiO_2) synthetized by plasma enhanced chemical vapor deposition (PECVD). On the other hand, this structure opens the possibility to transfer the epitaxial layer of the photoconductive material on another substrate (5) by Au-Au thermocompression bonding or by soldering with an Au-In or Au-Sn eutectic. The buried metal electrode can therefore also serve as a "bonding" layer between the epitaxial layer and a host substrate chosen for its thermal and/or electromagnetic properties.

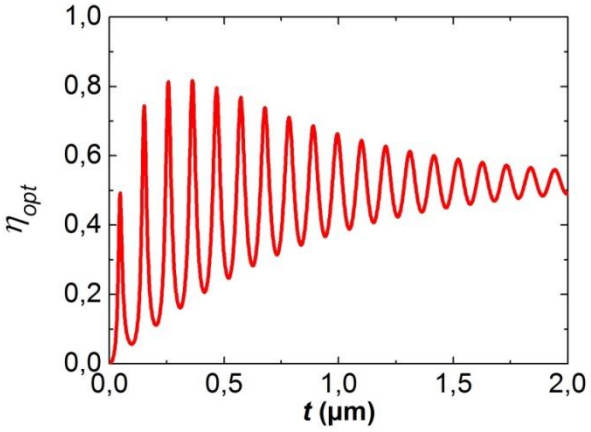

Figure 18: Calculated optical quantum efficiency versus active layer thickness (LT-GaAs parameters: $n = 3.7 + j0.09$ at λ_0=780 nm [53])

It can be shown that the resonant absorption peaks t_i of the cavity of complex refractive index ($n = Re(n) + jIm(n)$) illuminated by an optical wave of wavelength λ_0 are given by [54] :

Eq. 46

$$t_i = t_0 + i\frac{\lambda_0}{2Re(n)} \quad \text{with } i \text{ a positive integer}$$

The first peak occurs for a thickness t_0 which depends on the phase shifts induced by the reflections on the two mirrors of the cavity. On the other hand, if it is assumed that the lower mirror is perfectly reflective, it is possible to demonstrate that the optical absorption is maximum in the semiconductor if [48]:

Eq. 47

$$R_1 = (1 - e^{-\alpha t})^2$$

Where

- R_1 is the reflectance of the top mirror assumed to be lossless (composed here of several layers that are modeled by a single mirror).
- α is the absorption coefficient in the semiconductor.(i.e. $\delta_\alpha = \frac{1}{\alpha} \approx 0.68$ µm in GaAs at $\lambda_0 = 780$ nm and $\alpha = 4\pi Im(n)/\lambda_0$)

In Figure 18 is shown the optical efficiency calculated numerically by the of transfert matrix method [51] as a function of t in the case where the thicknesses of layer (1),(2) and (3) are 10 nm, 10 nm and 700 nm respectively. The substrate has no influence on the optical response since a gold layer of thickness greater than 150 nm is totally opaque at these wavelengths. Numerically, we find $t_0 = 47$ nm and $t_1 - t_0 = t_{i+1} - t_i = \frac{\lambda_0}{2Re(n)} = 105$ nm as expected ($Re(n) = 3.7$).

The absorption in the photoconductor is greater than 70% of the incident optical power for $t_{0<i<8}$ (see Figure 18). It is worth noting that even if the mirrors are not perfect, we find, as expected, a maximum absorption ($\eta_{opt} \approx 80$ %) for peaks obtained at $t_1 = 152$ nm and $t_2 = 257$ nm, the closest values to $t_{max} = 200$ nm obtained using Eq. 47 in the case where $R_1 \approx 50$ %) (reflectance calculated for the layer stack: 10 nm thick gold/infinitely thick GaAs)

Thus, compared to the planar structure in which $d = 2000$ nm, we obtain for $d_1 = t_1 = 152$ nm a theoretical improvement of a factor $\frac{2000}{152} \approx 170$ for the ratio G_0/P_{opt} while there is a degradation of η_{opt} of a factor 0.8 with respect to this same planar structure considering that the latter at a an optical quantum efficiency $\eta_{opt} = 100$ %.

In addition, the spectral width of the absorption resonance is compatible with the targeted application since we calculated that the absorption varies only from 1 to 2 % when the optical wavelength is increased from $\lambda_0 = 770$ nm to $\lambda_0 = 790$ nm which corresponds to a beating frequency $f \approx 10$ THz.

4.1.2 Experimental validation

4.1.2.1 Photoresponse

In order to carry out the experimental validation of the simplified model previously developed, we measured the photoresponse of an optical cavity photoconductor as a function of the inter-electrode spacing t on the same layer of LT-GaAs. We made this variation of thickness on the same sample by making a "bevel" etching of a 2.2-µm-thick LT-GaAs layer. By this method, we have obtained thicknesses ranging from 2.2 µm to 0.3 µm. We present Figure 19 the structure tested. The upper and lower metal electrodes are made of gold and serve as mirrors and bias electrodes.

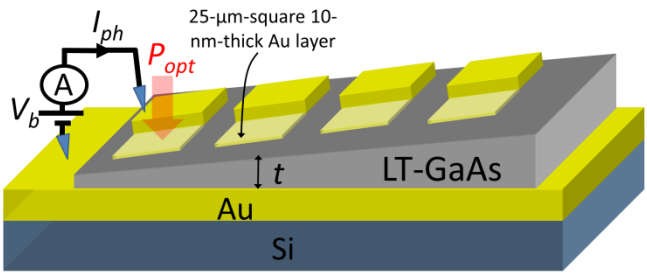

Figure 19: Experimental set-up aimed at photoresponse measurement

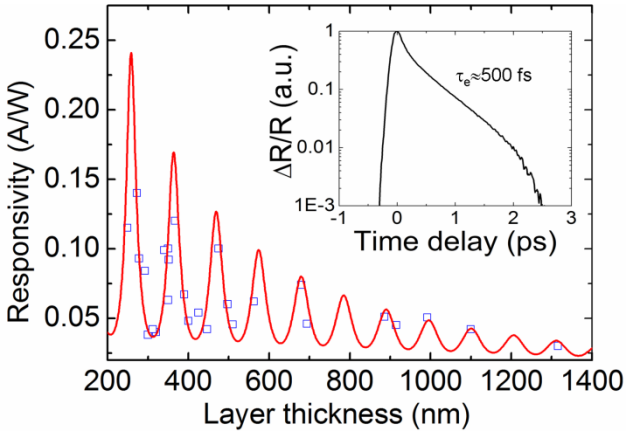

Figure 20: Theoretical (solid line) and experimental (in squares) photoresponses as a function of LT-GaAs layer thickness. In the inset is shown the transient differential photoreflectivity measured at λ=820 nm on the LT-GaAs layer [52].

In Figure 20 are shown the theoretical (solid line) and experimental (in squares) thickness dependences of the photoresponse measured for a constant mean electric field $\frac{V_b}{t} = 120\ \mathrm{kV/cm}$ and an optical power $P_{opt} = 9\ \mathrm{mW}$ at $\lambda_0 = 820\ \mathrm{nm}$. The $1/t$ dependence expected is convolved by the absorption peaks due to the optical resonance in the cavity. Experimental and theoretical details are further developed in Ref. [52]. It may be noted that for the peak located around $t = 250\ \mathrm{nm}$, a photoresponse of the order of $0.15\ A/\mathrm{W}$ has been measured, which is almost a ten times improvement with respect to the photoresponse of a planar photoconductor. In addition, a time-resolved photoreflectance experiment has been performed on the LT-GaAs layer after epitaxial transfer (shown in the insert of Figure 20), which shows that the photoresponse is high despite a lifetime of less than 1 ps.

4.1.2.2 Photomixing experiment in the 220-325GHz frequency band

4.1.2.2.1 Photomixer characteristics

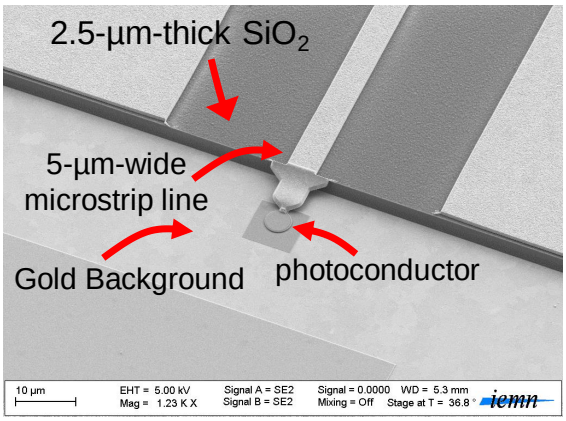

Figure 21: Optical cavity LT-GaAs photoconductor

In Figure 21 is shown a SEM picture of an optical cavity LT-GaAs photoconductor using the second absorption peak. It consists of a 160-nm-thick LT-GaAs layer sandwiched between two gold layers, which serve at the same time as bias electrodes and optical mirrors of the optical cavity. The 0.4-µm-thick buried gold layer is obtained thanks to the transfer of the LT-GaAs epitaxial layer onto a 2-in.-diameter silicon wafer. The upper bias electrode consists of a 20-nm-thick semi transparent gold layer and is linked by an air bridge to a 50-Ω thin film microstrip line patterned on a 2.55-µm-thick-SiO_2 layer. a 100-nm-thick silicon nitride layer is added to lower the top mirror reflectivity an to encapsulate the device.The fabrication process of the LT-GaAs optical cavity photoconductor is detailed in [52], [55]. In the table 1 are shown the main characteristics of the device

Diameter (µm)	Electrical Capacitance (fF)	f_{RC} (GHz) if R_L=50 Ω	Measured lifetime (fs)
4	11	290	400

Table 1: devices characteristics

4.1.2.2.2 Experimental Set-up

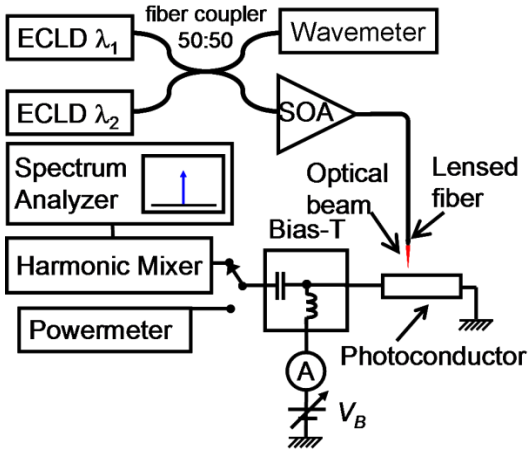

Figure 22: Experimental set-up. ECLD, external cavity laser diode; SOA, semiconductor optical amplifier. Lensed fiber: MFD = 5 µm.

A schematic overview of the experimental set-up is shown in Figure 22. A combination of half-wave plates and polarizers is used to ensure that the polarization of the two extended cavity laser diodes (ECLDs) are parallel and have equal powers. The optical beatnote is generated by spatially overlapping the two ECLDs ($\lambda_0 = 780$ nm) and used to seed a tapered semiconductor optical amplifier, the output of which is fiber-coupled. The optical wave is then focused into a 4 mm-wide gaussian spot by a lensed fiber. The wave generated in the photoconductor at the beat frequency is collected by a waveguide 220-325 GHz coplanar probe and sent to a sub-harmonic mixer driven by the spectrum analyser or to a powermeter (Erickson PM4).

4.1.2.2.3 Results

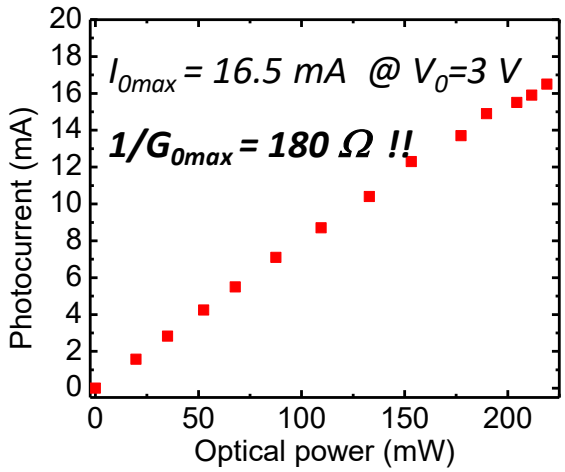

Figure 23: Photocurrent as a function of optical power V_b=3 V.

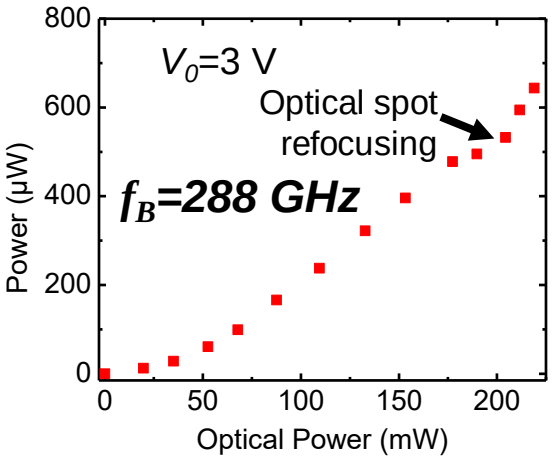

Figure 24: Output power at $\frac{\omega_b}{2\pi} = 288$ GHz and V_b=3 V.

In Figure 23 and Figure 24 are presented the results obtained in photomixing with this device[56]. As expected, we obtained a very low photoresistance, $\frac{1}{G_0} = 180\ \Omega$ instead of 10 kΩ with standard planar photoconductors (and 240 Ω with a previous generation using the third optical resonance peak

achieved at a thickness $t_3 = 280$ nm [57]). The maximum current of 16.5 mA has generated more than 600 µW at 288 GHz which once again validates the interest of reducing the thickness of the LT-GaAs layer at least for application in the lower part of the THz spectrum. It is worth noting that by using a matching circuit consisting of a ¼ wavelength transformer (see Figure 25) up to 1.8 mW of output power has been measured at 252 GHz with a 6-µm-diameter device delivering a photocurrent of 25 mA[58].

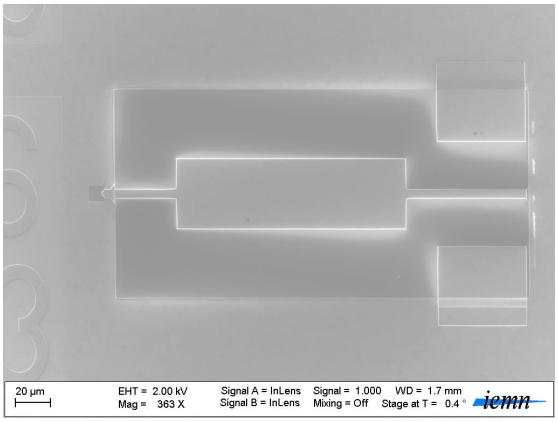

Figure 25: Top view of a 6-µm-diameter photoconductor coupled to the impedance matching circuit.

4.1.2.3 Output power estimation at 1 THz

diameter(µm)	C (fF)	f_{RC} (GHz) if $R_L = 50\ \Omega$	Photocurrent max (mA)	Current density(mA/µm²)	Output power (mW) at 50 GHz	Estimated power at 1 THz (µW)
2	2.7	1175	5.2	1.7	0.6	50
3	6.1	522	10.2	1.4	2.1	63
4	10.8	294	14.2	1.1	4.1	45
6	24.4	131	15.3	0.54	4.2	10
8	43.3	73	26	0.51	8.3	6

Tableau 2: Measured output power at 50 GHz and estimation at 1 THz as a function of device diameters. Current density are calculated by taking the maximum current density achieved experimentaly

In Table 2 are shown experimental output powers obtained at 50 GHz with different device diameters as well as an estimation (using the model developed in the previous part) of the achievable power at 1 THz when taking into account the two cutoff frequencies f_{RC} and f_τ = 400 GHz (measured lifetime τ = 400 fs). But it should be noted that, without any adaptation circuit, we can expect more than 50 µW of output power in a 50 Ω load at 1 THz with an optical cavity LT-GaAs photoconductors of diameter *d* = 3 microns and *d* = 2 microns. It can also be seen that the current

densities obtained (> 160 kA/cm²) are extremely high and it will probably be difficult to go much further. The largest diameters (*d* = 8 µm) photoconductors generating generate up to 8 mW at 50 GHz are logically less efficient at higher frequencies.

4.1.2.4 *Frequency down conversion using an optical cavity LT-GaAs photoconductor*

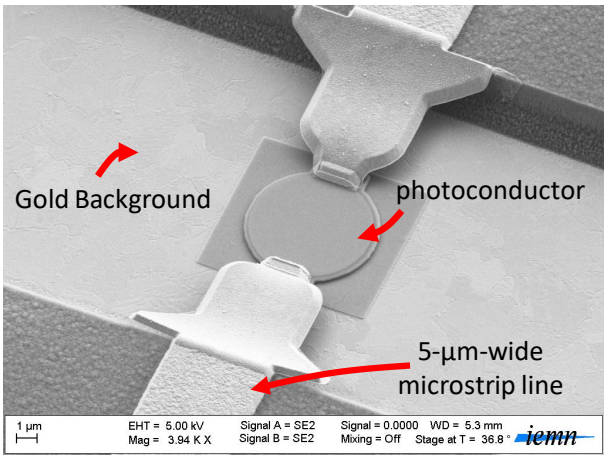

Figure 26: SEM micrograph of an optical cavity LT-GaAs photoconductor linked to two 50-Ω thin film microstrip lines.

As already presented, it is also possible to use a photoconductor to down-convert a signal of frequency f_{THz} to a lower frequency f_{IF} compatible with the digital acquisition and signal processing systems. This is achieved by setting the optical beatnote frequency f_b such that $|f_{THz} - f_b| = f_{IF}$. It can be seen as a heterodyne mixer using a photonic oscillator. This mixing between a THz wave that polarizes the photoconductor and the optical beatnote that modulates the carrier density is possible because a photoconductor has no internal electric field unlike a photodiode. In Figure 26 is shown a photoconductor with two microwave accesses fabricated in order to assess the potential of the optical cavity photoconductor when used as mixer. This study has been performed by using a photoconductor of thickness *t* = 160 nm and of diameter *d* = 4 µm (see Table 1).Down-conversion of waves up to 325 GHz has been carried out by using multiplier chains. At each frequency point, we adjust the emission wavelength of one of the two laser diodes to have an optical beat frequency f_b such that $|f_{THz} - f_b| = 400$ MHz. A waveguide coplanar probe was used to inject the THz signal while the IF signal was collected by a 0-67 GHz coplanar probe and sent to a spectrum analyzer.

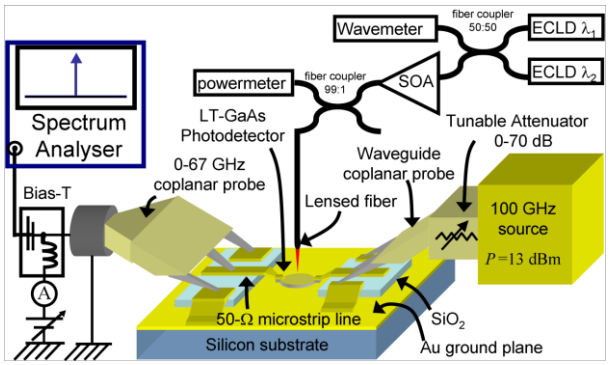

Figure 27: Down conversion experimental-set-up

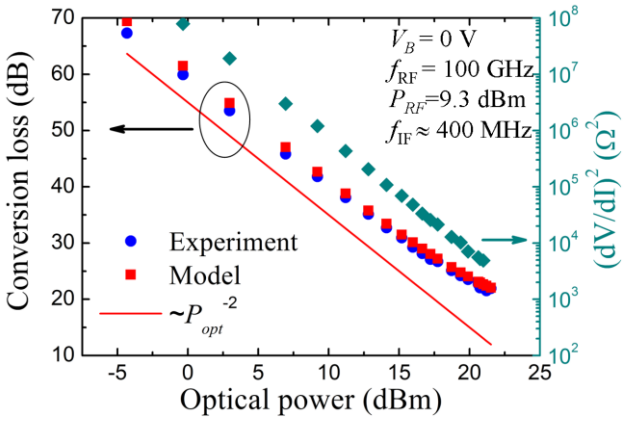

Figure 28: Conversion loss and (1/G0)² as a function of the optical power (P_{opt})

The conversion losses defined by $L = \frac{P_{THz}}{P_{IF}}$ of the order of L = 22 dB at 100 GHz and L = 27 dB in the 220-325 GHz band have been measured with an optical pump power of 100 mW. As expected, The conversion losses decrease when the optical power and therefore the photoconductance increases (see Figure 28). The electrical model of the experimental device shows that in the present case, with a load impedance (Z_L) and an internal source impedance such as $Z_s = Z_L$ and without THz and IF filters, (unlike the calculation made previously) the conversion loss is [25]:

$$L(dB) = 20\log\left(\frac{(2+Z_L G_0)^2}{Z_L G_0}\right)$$

which has a minimum L_{min}=18 dB when $G_0=2/Z_L=Z_s//Z_L=(25\ \Omega)^{-1}$. This corresponds to the impedance matching between the photoconductor and its load impedance. From the above relationship, $L \propto 1/G_0^2 \propto 1/P_{opt}^2$ when $Z_L << 1/G_0$ and saturates when $1/G_0 \approx Z_L$. Experimental results shown Figure 28 are in good agreement with this theoretical calculation. The losses related to the electrical capacitance and the carrier lifetime are of course neglected, assumption which is no longer valid at 300 GHz, which explains the higher conversion loss obtained (L = 27 dB).

4.2 UTC Photodiodes

UTC photodiodes for THz applications have active area of the order of 10 µm^2 to limit their electrical capacitance. At this scale, the contact resistance between metal and semiconductor may become a major issue. Vertically illuminated PDs using a metallic ring-based contact for mm-waves cannot be exploited efficiently anymore at THz frequencies due to the high contact resistance[59]. Most current photodiode designs for applications above 100 GHz therefore use a fully metallized top contact and backside illumination through the substrate[18], back-side illumination through a refracting facet [42], [60] or travelling wave structures using an edge-facet or waveguide illumination [45], [46] These

illumination schemes are cumbersome and make on-wafer measurements or integration with lens-coupled THz planar antennas very challenging, especially as compared with front side illumination.

In this context, has been proposed recently[19] a semi-transparent top contact based on a metallic layer with sub-wavelength periodic apertures covering a large fraction of the diode surface, resulting in a small contact resistance, while still maintaining a high transmittance at 1.55-µm-wavelength polarized light. This approach paves the way to efficient and powerful photomixers using front-side illumination. The proposed contact can be used with the same epilayer and mesa topology than a standard UTC-PD. Moreover, this structure is well suited to be integrated in an optical cavity by integrating the semiconductor layers between this semitransparent contact as top mirror and a buried metallic layer as bottom mirror to form a resonant cavity enhanced UTC (RCEUTC).

4.2.1.1 Nano grid top contact electrodes

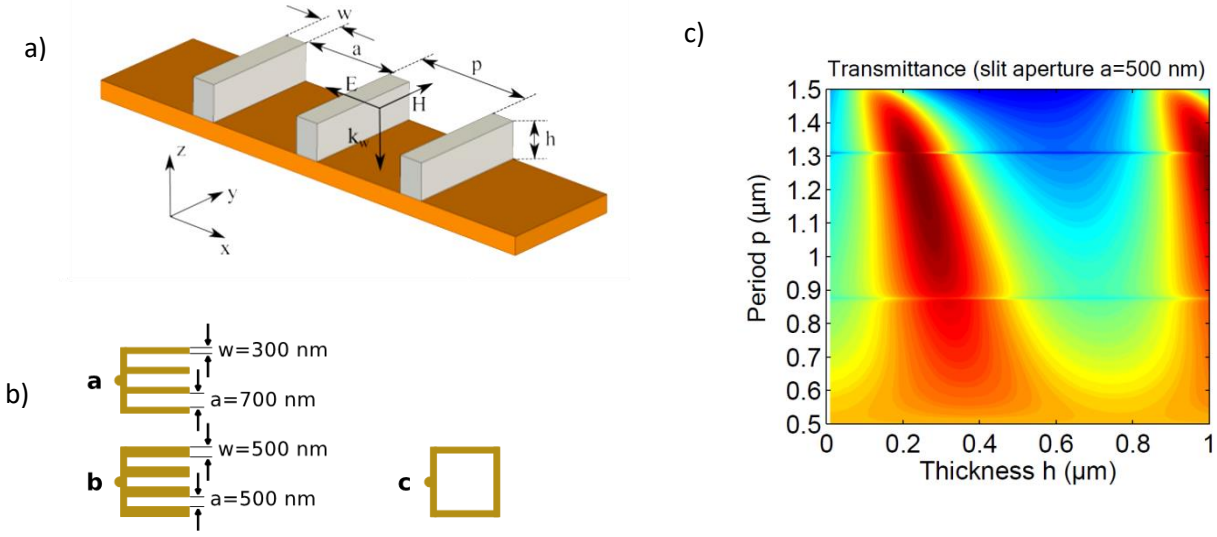

Figure 29: Design of the nanostructured contact. (a) Geometry of the metallic semitransparent nanostructured contact. (b) Schematic of the fabricated semitransparent contact geometries. The c-type contact without nanostructure serves as comparison. Calculated transmittance of an infinite surface of parallel strips of a perfect electrical conductor on InGaAs (n = 3.55), illuminated by a p-polarized plane wave with 1.55 µm wavelength. The calculations are performed using the coupled-mode-method and the single-mode approximation.

The topology of the device is presented on Figure 29. The semi-transparent contact consists of parallel metallic strips of width *w=p-a*, with period *p*, aperture *a*, and metallization height *h* (Figure 29a). The transmittance of an infinite surface of such strips can be calculated using quasi-analytical techniques such as the coupled-modes method [61]. Figure 29c shows the transmittance of a p-polarized plane wave of wavelength λ*=1.55 µm* through such a surface of strips on $In_{0.53}Ga_{0.47}As$. For a choice of the semi-transparent contact parameters *(a, p, h)* lying in the high transmittance regions (red regions) it is possible to achieve values higher than 90%, even with 50 % of the surface covered by metal, for example at *a=0.5 µm*, *h=0.3 µm*, and *p=1 µm*.

4.2.1.2 UTC photodiodes using nano-grid top contact electrodes

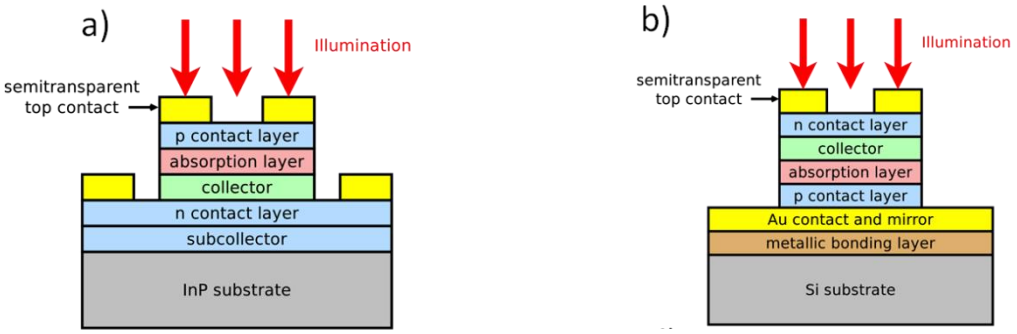

Figure 30: Fabrication of the PD. (a, b) Schematic cross section of the fabricated devices, (a): UTC-PD, (b): RCEUTC-PD, fabricated after wafer-bonding of the epitaxial layers to Si substrate and removal of the original InP substrate by wet-etching.

Two parameter sets are selected for device fabrication (Figure 29b): (a) *a*=700 nm, *p*=1 µm, *h*=300 nm *A.3.5* (~80% transmittance) and (b) *a*=500 nm, *p*=1 µm, *h=300 nm A.3.5* (~90% transmittance). Additionally, diodes without strips, but with (c) the contact metallization on the border of the mesa are fabricated for comparison. In that case, a 63% transmittance is obtained, corresponding to the air/semi-conductor interface (n~3.2). Moreover, the semi-transparent contact allows the fabrication of optical cavity UTC Photodiodes by inclusion of a mirror below the active photodiode layers, improving the photoresponse of the devices [50][58]. Schematic cross-sections of the devices are shown in Figure 30. All diodes are fabricated from the same epitaxy with 150 nm absorption layer and 100 nm collector layer, and a square geometry of 3×3 µm², 4×4 µm², and 6×6 µm² are chosen for the mesa. SEM images of the two device types are shown in the Figure 31.

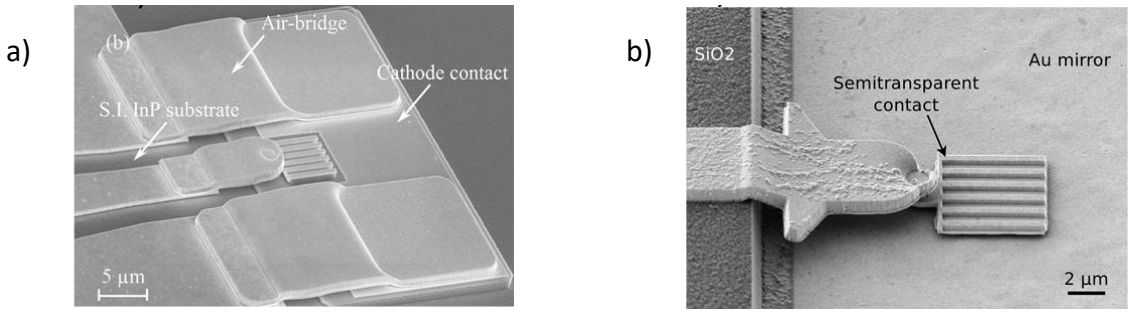

Figure 31:a)SEM image of UTC-PD integrated with CPW, and (b) SEM image of RCEUTC-PD, integrated with conductor-backed-CPW lines on SiO_2 for on-wafer measurements.

4.2.1.3 Photoresponse measurement

In order to illustrate the enhancement of dc responsivity and THz output power of the RCEUTC, the PD's were characterized by on-wafer measurements in which the devices are illuminated by using a lensed fiber providing an optical spot of 3 µm (see ref [19] for further details). In the following, the RCEUTC devices are indicated by capital letters. The dc photoresponse $\mathcal{R}$ of the larger devices (6×6 µm²) are shown in Table 3. The lowest photoresponse corresponds to the device without finger contact (c6, see Figure 29b), and improves by nearly 30% adding the semi-transparent contact with

300 nm wide fingers (a6) and 40 % by the 500 nm wide fingers (b6). By including the metallic mirror through wafer bonding, a resonant cavity is created, as evidenced by the photoresponse of the A6 and B6 devices (see Figure 32). The photoresponse is in both cases improved by a factor larger than 3 compared to the c6 device.

Diode	a6	b6	c6	A6	B6
R (mA/W)	58	65	49	167	255

Table. 2. Dc photoresponse at 1550 nm of 6×6 µm² UTC-PD and RCEUTC-PD devices under illumination of a single laser at low power of 320 µW.

4.2.1.4 THz power generation by photomixing

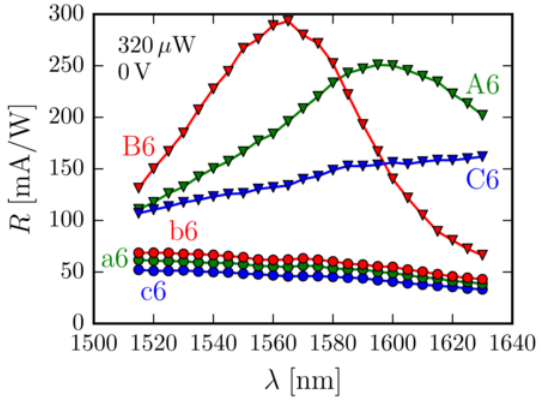

Figure 32: Experimental comparison of photoresponse of UTC-PD devices and RCEUTC-PD over 1510-1630 nm range

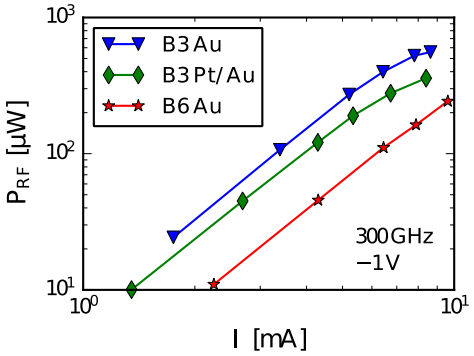

Figure 33: RF power generated at 300 GHz by various B-type photodiodes for 3×3 µm² (B3) and 6×6 µm² area (B6).

Finally, the photodiodes have been tested up to the saturation regime. In Figure 33, the linear and saturation regimes of the output power can be observed at high photocurrents in the devices with 3×3 µm². The saturation is due to space charge screening at high current densities in the collector region [62]and temperature dependence of the electron transport properties. The larger device (6×6 µm²) does not reach saturation at the measured photocurrents due to the smaller current densities, and the available optical power was not high enough to reach the saturation regime. Also, we compared two metal stacks for top-contact B3, Pt/Au and Au. The B3 Pt/Au device generates lower RF power than the B3 Au device at the same photocurrent due to the contact resistance which is larger for Pt than Au on n-InGaAs. The saturation effects can be reduced by applying a higher bias voltage, and by slightly increasing the distance between lensed fiber and diode, which reduces the maximum current density in the center of the PD at the cost of a lower photoresponse. Upon defocalisation, reducing the photoresponse by 0.5 dB, an RF power just above 750 µW at 300 GHz has been measured from a B3 device at -1.2 V bias, 83 mW optical power, and 9.8 mA photocurrent. It shows that, to the best of our knowledge, the RCEUTC presented here generates the highest power for a single device at 300 GHz. These results show the real advantage of using an optical cavity

consisting of a buried metallic layer (instead of a bragg reflector for example) in the case of photodiodes by improving also the electrical properties (contact resistance) and the thermal properties of the device.

5 THz Antennas

In the THz range, the standard rectangular metallic waveguides are lossy and the integration with a photodetector can be very challenging. The use of an integrated antenna in order to radiate directly a THz wave in free space using the generated THz currents has allowed for overcoming this difficulty. We will first focus on standard planar antennas which were the first used and then on micromachined antennas requiring more technological development.

5.1 Planar Antennas

The most popular terahertz antennas consist of planar conductors patterned directly on the semiconductor on which the photoconductor is made. Most of the common planar antenna geometries have been tested yet, equiangular spiral [8], logarithm-periodic [12], [63] or bow tie [64] as broadband antennas and dipole [64], [65], slot [65], dual-dipole and dual-slot [20], [41] as resonant antennas.

Broadband antennas are generally chosen in order to take advantage of the very large intrinsic tunability of the photomixing source. In theory they can have a purely resistive impedance over a wide frequency range. Two main principles can be used to obtain a frequency independent antenna. Firstly, the Rumsey principle stipulates that the antenna has to be described entirely by angles [66] [67], as the bow tie or the equiangular spiral antenna. If an infinite antenna verifies the Rumsey principle the shape of the antenna remains the same regardless of the scale at which it is viewed (in the case of the spiral a rotation might be needed). Another principle which is useful to estimate the impedance of an antenna is the Babinet's principle. It states that: $Z_{Ant}Z_{Comp}=Z_s^2/4$ where Z_{Ant} is the impedance of an antenna, Z_{Comp} is the impedance of its complementary, Z_s is the impedance of free space of the surrounding medium[68]. A particular case is interesting when an antenna is equivalent to its complementary: it is self-complementary (a classical example is the infinite bow-tie antenna with an angle of 90°), in this case the impedance of the antenna is purely resistive, independent of frequency and equal to $R_A=Z_0/2\approx188.4\ \Omega$ in vacuum. When a planar self-complementary antenna is patterned at the boundary between two different media of relative permittivity ε_{r1} and ε_{r2} the impedance becomes $R_A=Z_0/(4\varepsilon_{eff})^{1/2}$, where ε_{eff} is the effective dielectric

constant: $\varepsilon_{eff}=(\varepsilon_{r1}+\varepsilon_{r2})/2$. Let's focus on the two most common broadband antennas for photomixers: the equiangular spiral antenna [69] and the logarithm-periodic antenna [70].

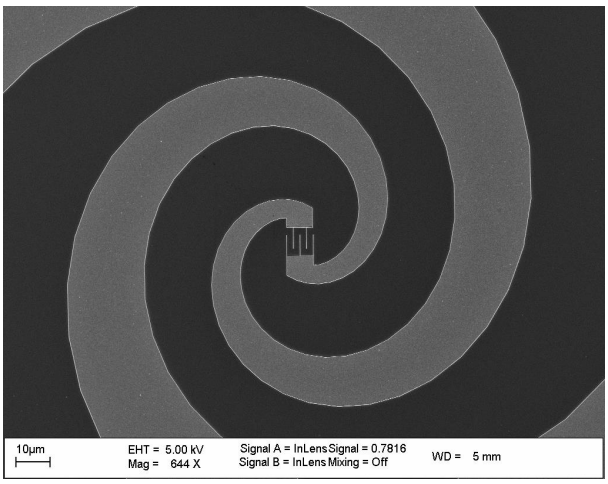

Figure 34: SEM picture of an equiangular spiral antenna

The equiangular spiral antenna patterned on a GaAs substrate (see Figure 34) used by Brown et *al*. [8], is self-complementary. Contrary to what was supposed in the previous paragraph practical antennas are finite. They cannot be infinitely large then a low frequency cut-off appears when the overall length of the spiral arm is approximately equal to the radiation wavelength. They cannot be also infinitely small close to the center. The smallest inner radius in the center of the spiral defines the high frequency cut-off. Between these two cut-off frequencies the previous calculation can be used to approximate the radiation resistance in the working bandwidth. For GaAs, ε_r=12.9 and then $R_A\approx 71\ \Omega$. In this bandwidth the radiated field is circularly polarized, the type of polarization depending on the direction of winding of the spiral. The size of the antenna can be chosen to have a frequency cut-off around 0.1 THz. The high frequency cut-off is limited by the photodetector dimension. For instance, it has been shown that for a 8x8-µm² LT-GaAs planar photoconductor at the center of a spiral antenna, the radiated field is no more circularly but linearly polarized parallel to the fingers of the interdigitated electrodes above f=0.6 THz [71], [72]. It shows that the standard design of the spiral antenna is rapidly inefficient at high frequency and that the terahertz wave is preferentially radiated by other conductive parts even if the guided wavelength $\lambda_g=c/(f\times\varepsilon_{eff}^{1/2})\approx 190$ µm is much larger than the inner radius. This observation is consistent with the steeper decrease than expected of the power radiated by the spiral antenna-coupled-photomixers [73].

The log-periodic antenna can be seen as an array of tooth-shaped resonant dipole, attached perpendicularly to the bow-tie arms. This geometry doesn't fulfilled the Rumsey principle, but it damps the resonance brought by the finite length of a real bow-tie antenna [70]. The operation bandwidth is defined by the smallest and the largest teeth. At each resonant frequency, the radiated

field is linearly polarized parallel to the resonant tooth. The frequency dependency of the radiation impedance is clearly not as smooth as that of the spiral antenna. It impacts also the frequency dependency of the output power of log-periodic antenna-coupled-photomixers [63].

The radiation impedance of the planar broadband antennas on semiconductors is generally below 100 Ω. As seen before, higher antenna impedances can be a way to improve the output power and the efficiency of the photomixing process. Record output power have been achieved, whatever the type of photodetector, with resonant antenna whose impedance can reach some hundreds ohm at the resonance [20], [41], [45], [74]. However, it is worth noting, that improvements are achieved thanks to the higher antenna impedance, but also thanks to a matching condition that can obtained near the resonance in a narrow band: the capacitance of the photodetector is compensated by an inductive behavior of the antenna. A matching circuit can be also added in order to increase the bandwidth.

The radiation pattern of a planar antenna on a high permittivity substrate is very different of the same antenna in vacuum. In this case, the most part of the electromagnetic energy is radiated into the semiconductor because of its high permittivity. If a standard substrate is used (a few hundreds of µm thick), guided electromagnetic modes are excited and trapped into the wafer (surface waves) [75]. The impedance of the antenna and its radiation pattern depend on the exact dimensions and shape of the substrate and tend to be very resonant. In practice the characteristics of the antenna are difficult to control. In order to avoid this behavior, the standard solution consists in applying a "substrate lens" to the backside of the substrate [76], [77]. It is the analog of the solid immersion lens used in microscopy; ideally the lens should have the same permittivity as the substrate. For a GaAs substrate ($n_{GaAs}\approx3.6$), high-resistivity silicon ($n_{HRSi}\approx3.42$) spherical lenses are generally used because they are easier to manufacture and handle. Following the concepts of geometrical optics, at high frequencies, the planar antenna can be approximated as a point source. In this case perfect stigmatism is obtained for the Weierstrass case: the height of the truncated sphere is $(1+1/n)R$ where R is the radius of the spherical surface of the lens. For HR Si the height should be 1.29 times the radius of the sphere, they are called hyperhemispherical lenses. Thanks to these lenses the divergence of the beam is largely reduced but a better collimation can be achieved using an extra lens or parabolic mirror. The refractive index of semiconductors being high, hemispherical lenses (height equal to the radius) can also be used with a slightly reduced efficiency. In all case some waves are still trapped in the substrate + lens system because of the Fresnel reflections at the silicon/air boundary and broadband anti-reflection coatings are not available. In practice the substrate lens is the simplest way to reduce the trapped waves of planar antennas but its spatial alignment is critical, particularly at high frequency, and it requires good translation stages with micrometer screws. The substrate lens can be bonded after active alignment but precautions

must be taken to avoid gaps between the lens and the substrate that can induce parasitic reflections. Another constraint of the substrate lens is that the photomixer cannot be illuminated from the backside of the substrate.

The exact calculation of the radiation pattern of planar antennas coupled to a high permittivity substrate lens is still a difficult problem and only a few reports give simulations and practical measurements [78], [79],[80]. The following section deals with the few attempts of alternative antennas or waveguide structures which have been done in order to overcome the limits of the lens-coupled planar antenna.

5.2 Micromachined Antennas

Antenna on semiconductor membranes have been proposed [81] but results have been disappointing because of the low thermal conductance of the membrane, which limits the maximum optical power that can pump the photomixer. More interesting results have been obtained with a transverse electromagnetic horn antenna (TEM-HA) integrated with both a LT-GaAs photoconductor [37] and with a UTC-Photodiode [42].

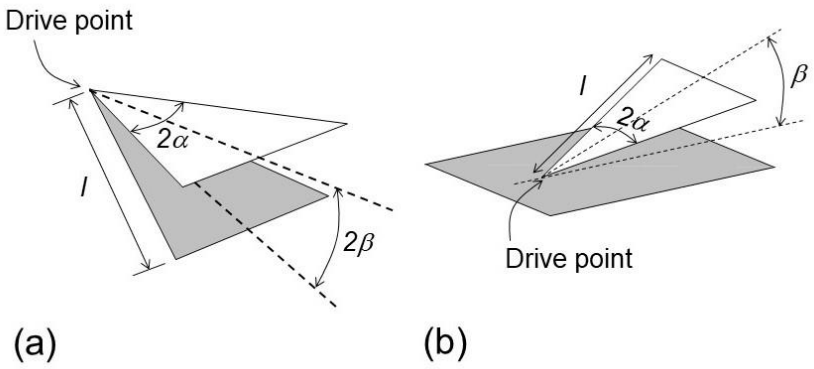

Figure 35: Geometry of the TEM-HA (a). Geometry of the monopole configuration of the TEM-HA (b).

A TEM-HA (Figure 35) can be seen as a flat version of a truncated section of a TEM biconical antenna[68]. It is an end-fire travelling wave antenna consisting of two triangular conductive sheets of angular width 2α separated by an angle 2β. Entirely defined by angles, the infinite antenna respects the Rumsey principle. In practice, the low frequency cut-off is defined by the length of the triangle. For the particular case β =90° the TEM-HA is equivalent to a bow-tie antenna. The monopole configuration of the TEM-HA, with a ground plane at the symmetry plane is shown in Figure 35. The 3D shape of this antenna is simpler and the conductive plane is used to prevent the radiation from spreading in the substrate (shielding).

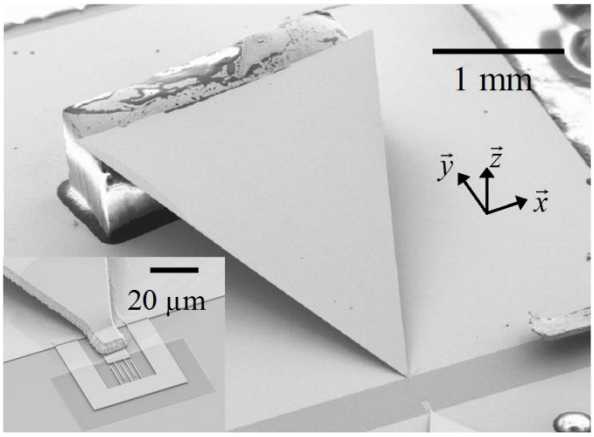

Figure 36: SEM picture of a THz Horn antenna

In Figure 36 is shown a SEM picture of a TEM-HA Horn monolithically integrated with a LT-GaAs photoconductor [37]. The metallic triangle has been patterned on a sacrificial layer and then lift up to the desired height (here *h*=800 µm) and brazed to a metallized polytetrafluoroethylene (PTFE) block.

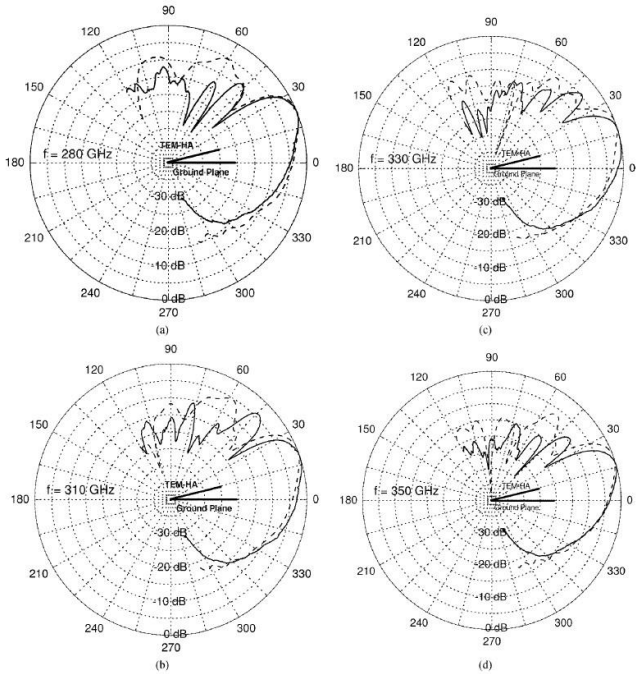

Figure 37: E-plane radiation patterns of the TEM-HA: comparison between experimental results (full line) and simulations (dashed line) at 280, 310, 330 and 350 GHz (

Radiation patterns have been calculated [82] and a good agreement with measurements has been found [83] (Figure 37). The TEM-HA radiates linearly polarized waves directly in free space and thus resolves most of the problem of the lens-coupled planar antenna, but its fabrication needs a post-process packaging step, which is likely to limit its diffusion.

To conclude this section about antennas for photomixers, it must be noted that even if the integrated antennas are necessary for most of spectroscopy applications they have a limited efficiency especially at the highest frequencies. Improvements are still needed in this domain.

Another aspect is that the evaluation of the absolute power produced by a photomixer integrated with an antenna is a difficult task: impedance variations, collection efficiency and back reflections limits generally the power and the precision to which it can be measured (as mentioned in the last part of this chapter) . The record output powers, which reach the milliwatt level, at least in the low frequency range, have been reported with waveguide-coupled-photomixers [43][18] or by means of waveguide-coplanar probes coupled to waveguide power meters [44][57].

6 Characterization of photomixing devices

6.1 On Wafer characterization

Since the early applications of THz waves, many of the photoconductive devices and photodiodes have been used and characterized in free space, driven by applications or just by the fact that wafer-level characterization has an overall quite high cost. However, accurate characterization of devices for modelling generally requires on-wafer testing. This can be conducted at several frequency ranges, however depending on the probe used the band can be reduced. On-wafer measurements and device modelling is generally done using coaxial probes up to 110 GHz that can provide 4 frequency decades usually when combining with coaxial vector network analyzers (VNAs). Recently, VNA coaxial extensions have now reached up to 220 GHz in a single sweep[84].However up to now, beyond 110 or 140 GHz, measurements are conducted mostly in waveguide configuration. In that case, the bandwidth is 1:1.5 related to the waveguide range. Definitions of usual waveguide bands can be found here [85]. The probe technology is frequency band depending: looking on high frequency measurements up to 500 GHz, probes integrated with micro-coaxial tips are available[86].Beyond 500 GHz, Picoprobes now also enables [87] measurements up to 1.1 THz, with micro-coax connection at probe tip. Recently, new probe technology was introduced[88] using micromachined silicon circuit at probe tip, and these devices enable wafer-probing up to 1.1 THz [89] (see Figure 38). This technology, thanks to the microfabrication techniques is scalable in frequency and enables up to now probing up to 1.1 THz. All of these probes have a footprint corresponding to a coplanar contact (Ground Signal Ground). To ensure a good signal coupling to the device as the wavelength is reduced, the “pitch” size, ie the physical length between signal and ground contacts as to be reduced accordingly. In the 140-220 GHz range a 100 or 50 µm GS distance is required. Beyond 220 GHz a pitch of 50 µm becomes mandatory and the distance is further reduced down to 25 µm for 325-500 or 500-750 GHz. The highest frequency band, commercially available for on-wafer testing is 1.1 THz, corresponding to WR1.0 waveguide (750-1100 GHz). Looking on photomixer on-wafer testing, the

Figure 39a gives an over view of a typical characterization setup for on-wafer measurements [91].

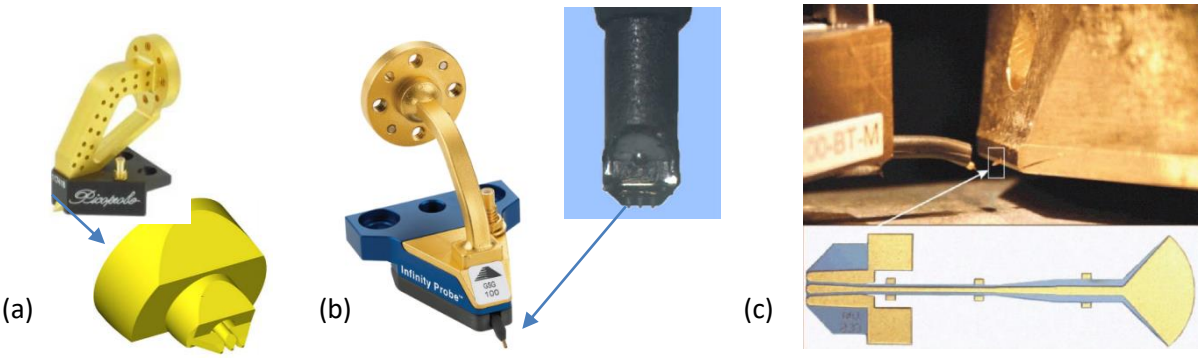

Figure 38: Different probes technologies: GGB probes [87] **(a), Infinity-micro-coax (b), up to 500 GHz**[86] **and micromachined probes (c)** [90]**.**

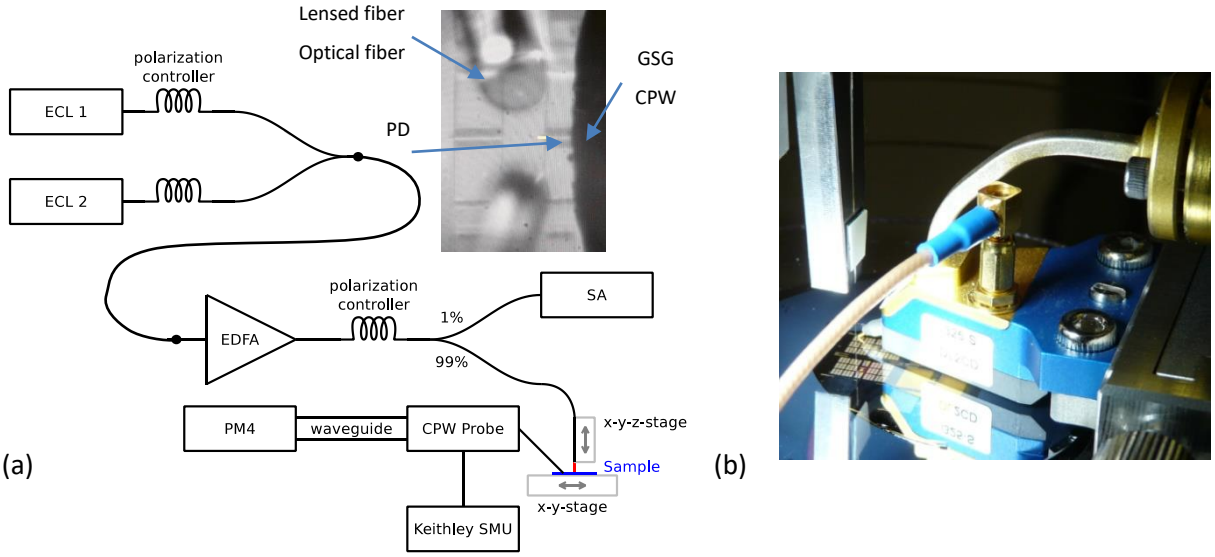

Figure 39: (a) Experimental setup for photomixing at wafer-level. (b) Photograph of the probe station showing the wafer-level photomixers, the fiber optic injection and the waveguide-probe.

In this kind of photomixing setup, two external cavity lasers are used as sources for continuous-wave (cw) photomixing. A fiber coupler is used to couple the two detuned laser wavelengths and a polarization controller to adjust the polarization of the optical wave injected inside de photomixers. Indeed, depending of the photomixer structure used the sensitivity can be polarization dependent and, in that case, the polarization of the two beams has to be carefully adjusted. Generally, the laser powers, considering the extra losses of fiber components (polarization controllers, couplers, …) are not reaching the required power to properly feed the photomixers, then optical dual-frequency signal is often injected inside an erbium-doped fiber amplifier (EDFA).

As the EDFA gain is generally depending of the wavelength, a fraction of the optical power is injected into optical spectrum analyzer (OSA) to monitor the spectrum. In this spectrum, the difference

frequency of the lasers has to be monitored during the during RF power measurements. At the end, the optical signal is injected inside the photomixing device with a lensed fiber. The spot size is also depending of the photomixer structure, for the example given here, it is around 3 µm, linked to the UTC-PD diameter. The

Figure 39b gives a photo of InGaAs/InP photodiodes during wafer-level testing. This example of measurement uses a waveguide coplanar probe in WR3.4, with integrated bias-Tee (Cascade microtech infinity i325). Usually, the DC output of the bias-Tee is connected to a source meter to bias the device while measuring the photocurrent, meanwhile RF output (ground–signal–ground, 50-µm pitch) of the probes is feeding a waveguide-based power-meter, in that case this is a PM5 from VDI. This power meter has the advantage to give an absolute power level measurement, and thanks to the waveguide coupling, the signal is properly coupled in the detector. However, there are two limitations: i) the signal frequency range is limited to the probe/waveguide bandwidth and ii) the electrical response of the probe (amplitude and phase) has to be accurately known to evaluate the photomixer performances. A first example of the frequency dependence of the output power in the 220–325-GHz band is shown in Figure 40. While on the range 220-270 GHz the photodiode roll-off is appearing, beyond 270 GHz some ripples are affecting the measurements. These oscillations are due to the frequency dependence of the load impedance presented by the coplanar probe. This roll-off is due to an inductive part of the load impedance, which increases with frequency and partially matches the load the device and access pad capacitance.

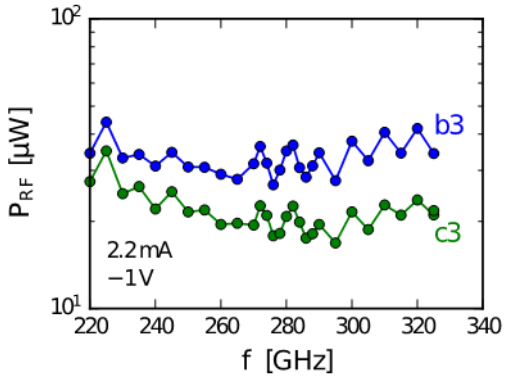

Figure 40: Frequency response example of a UTC-PD [91].

A second example of UTC-photodiode (same UTC size) output power measurement is given by the frequency evolution (Figure 41a) and linearity (Figure 41b) of the device at 300 GHz. this measurement is done this time using a micro-machined probe, and the spectral evolution of the output power is not exactly the same, partially linked to the loading probe effect. On-wafer testing

thus requires a good knowledge of the probe effect on the device as absolute power measurement is concerned.

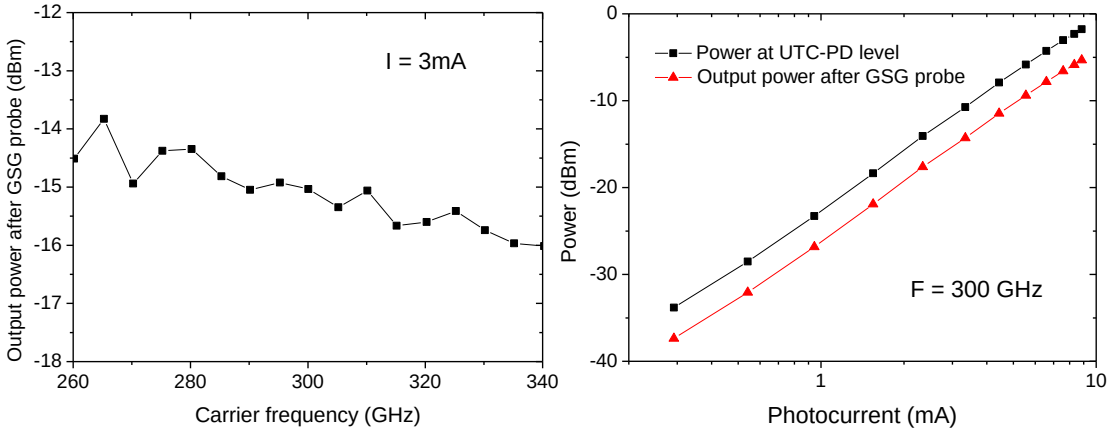

Figure 41: Frequency response example of and device linearity.

6.2 Free Space characterization

Even if on-wafer measurement is generally well suited for device modeling and cut-off frequency analysis, characterization up to the THz range is enabled using photomixer + antenna structure. In that case the THz signal is radiated directly into the free space and different power-meters can be used.

A large part of the THz photomixing devices have been integrated with different antenna types. This can be planar antennas (bow-tie, spiral, dipoles) as well as integrated antennas used as transitions towards waveguide structures. In that case, it is generally difficult to accurately measure the output power levels because of the radiation in free space of the THz signal. In this case, the measured performance is the mixing of the photomixer + antenna structure, not the photomixer itself. Using planar antennas, generally associated with a silicon lens, the signal power level is mostly dependent of the silicon lens alignment. It can also be affected by the presence of an air gap between substrate and lens, leading to deleterious frequency response and echos in time-domain. Looking on detector side, several solutions exists today: pyro-electric detectors, Schottky diodes integrated with silicon lenses, as well as free-space detectors with traceable calibration from PTB [92], as well as golay cells or Thomas Keating detector [92]. Additional information can be found in [93].

The

Figure 42 hereafter gives an example of the free-space characterization of a broadband non resonant UTC-PD integrated with a TEM-horn antenna[42], this UTC is then associated to a set of lenses to feed a quasi-optic Schottky module for THz reception. As can be seen on the frequency response, even if the spectral response of the device is broadband, some ripples in the curve can easily reach 3 dB variations at specific frequencies, coming from stationary wave (S.W.) effects between the THz source and receiver. This experimental limitation is often encountered in such kind of measurements, and in that case, the use of isolators could be helpful. In addition, as soon as the power-meter or detector is designed to reduce the level of back-reflection at the detector input, these S.W. can be greatly reduced. Generally speaking, the power measurement in free-space configuration is still a challenging issue in the sub-mm or THz range and intensively investigated by the THz researchers.

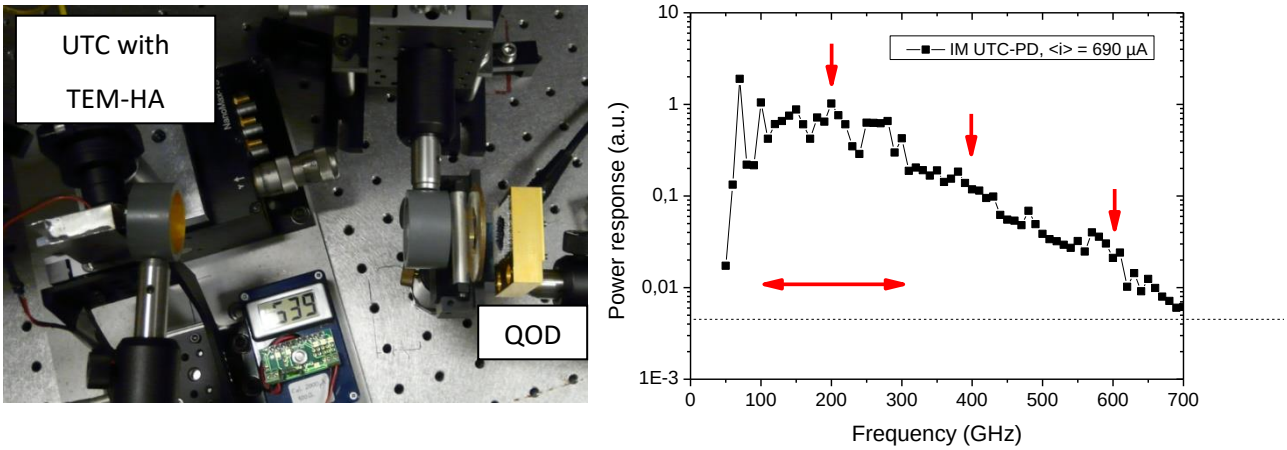

Figure 42: Example of free space UTC-PD measurement using a Schottky quasi-optic detector[94]. Some ripples on the frequency response are observed due to the stationary waves between THz source and receiver.

7 Exercices

A :Photodetector theory :

A1) By assuming that each photon incident on a photodetector results in an electron-hole paire reaching the contact electrodes, give the maximum photoresponse achievable as a function of the photon wavelength.

A2) Demonstrate that the Photoresponse×bandwidth product of a THz photoconductor based on a low-carrier lifetime semiconductor is independent of the carrier lifetime if we neglect the electrical capacitance.

A3) Calculate the photoresponse at λ=780 nm of an ultrafast photoconductor based on a 1 µm-thick LT-GaAs layer (lifetime τ=500fs) with contact electrodes separated from *s*=1 µm by assuming that :

- There is no reflection of the incident light at the top and bottom interfaces of the layer

-Absorption depth in GaAs at λ=780 nm :$\delta \approx 0.7$ µm

-photocurrent results only from the electron drift at a velocity v_s=10^7cm/s.

A4)Explain why a uni-travelling carrier photodiode has better current saturation bandwidth properties.

A5)Give the physical origin of the response time of a UTC photodiode.

A6) Plot the ratio conduction current (i_c)/average optical power (P_{opt}) of an UTC PD of surface 10µm^2 illuminated by a optical beatnote as a function of the beatnote frequency:

UTC layer properties :

- a 150-nm-thick absorbing InGaAs layer with a gradient composition.

-A 300-nm-thick InP collector layer in which the electron are assumed to drift at their overshoot velocity.

The absorption depth in InGaAs is $\delta \approx$1µm.

B : Photomixing model :

1 : Ultrafast Photoconductor

We study a photomixing source based on a planar photoconductor of capacitance *C*=5 fF, photoresponse 0.02 A/W at V_b =5V pumped by an incident optical beatnote of average power P_{opt}=50 mW. The carrier lifetime of the photoconductive material is τ=400 fs. It is assumed that it behaves as a perfect photoconductance up to V_b. The impedance of the antenna coupled to the photoconductor is equal to 70 Ohm (purely radiative).

B1.1) By using the equivalent electrical model, give the expression of the output power as a function of the frequency.

B1.2) Plot the output power as a function of the frequency from 10 GHz to 1 THz.

B1.3) Calculate the optical power required to reach the impedance matching between the photomixing source and the antenna. Is it realistic?

2 : UTC Photodiode

The UTC PD of the question A6 is pumped by an optical beatnote at λ=1550 nm of average power P_{opt}=30 mW which is assumed to reach without loss the absorption layer. The impedance of the antenna coupled to the photoconductor is equal to 70 Ohm (purely radiative).

B2.1) By using the equivalent electrical model, give the expression of the output power as a function of the frequency.

B2.2) Plot the output power as a function of the frequency from 10 GHz to 1 THz.

B2.3) Is it possible to achieve the impedance matching condition.

C: Antennas

We want to integrate a photoconductor with a spiral antenna.

C1) Calculate the impedance of an infinite self-complementary THz spiral antenna fabricated on a semi-infinite quartz substrate (refractive index of quartz in the THz range: 2.0)

C2) Is the spiral antenna on quartz more favorable than the same antenna on GaAs from the point of view of impedance matching ? (you can repeat exercise B1 with this new antenna impedance)

8 Solutions

A1 : Photons flow (F_{ph}) =incident optical power (P_{opt})/photon energy (E_p)

E_p =hc/λ

h :plank constant,

c =light velocity

E_p (J)=1.24×*e*/λ(µm)

e=1.6×10^{19}C ;

dc Photocurrent (I_{dc})=*e*×F_{ph} = e× P_{opt} / E_p =λ(µm) × P_{opt} /1.24

Photoresponse= I_{dc} / P_{opt} =λ(µm)/1.24

A2 :

From Eq. 12

Photoresponse $\mathcal{R} = \frac{e}{hv}\eta_{op}\tau/\tau_{tr}$ with τ the carrier lifetime and τ_{tr} the carrier transit time and $\eta_{opt} = (1-R)(1-e^{-\alpha d})$ is the quantum efficiency (*R* the reflection at the Air/semiconductor interface).

Frequency Bandwidth $B = 1/(2\pi\tau)$ if we neglect the effects of the capacitance and if $\frac{\tau}{\tau_{tr}} \ll 1$

then $\mathcal{R}B = \frac{e}{hv}\frac{\eta_{op}}{\tau_{tr}}$

A3 :

By taking the expression given in A2:

$$\mathcal{R} = \frac{e}{hv}(1-R)(1-e^{-\alpha d})\,\tau/\tau_{tr} = \frac{\lambda(\mu m)}{1.24}(1-R)(1-e^{-\alpha d})\,\tau/\tau_{tr}$$

with $R = 0$, $\alpha = \frac{1}{0.7}\mu m^{-1}$ and τ_{tr} =s/v_s=10 ps

we find $\mathcal{R}$ =0.024 A/W.

A4: See section 2.2.2 Uni-Traveling-Carrier Photodiodes p. 13 for explanation.

A5: See section 2.2.3 Photocurrent generation p. 14.

A6: From Eq. 40 in p.15 we deduce

$$\frac{i_c(\omega)}{P_{opt}} = -\frac{e}{hv}(1 - e^{-\frac{W_a}{\delta}})\frac{1}{1 + j\omega\tau_a}\frac{\sin(\frac{\omega\tau_{tr}}{2})}{\frac{\omega\tau_{tr}}{2}}e^{-j\frac{\omega\tau_{tr}}{2}}$$

where δ=1 µm, W_a = 150 nm, because of the gradient composition $\tau_a \approx \frac{W_A}{v_d}$ with $v_d \approx 2 \cdot 10^7 \text{cm/s}$ in InGaAs. In the collector, the electrons are assumed to reach the overshoot velocity $v_{ov} \approx 4 \cdot 10^7 \text{cm/s}$, and then $\tau_{tr} = W_c/v_{ov}$ with $W_c = 300$ nm.

B1.1:

Eq. 29 p. 11:

$$P_{THz} = \frac{V_b^2 G_0^2}{2}\frac{G_L}{[(G_0 + G_L)^2 + (\omega_b C + B_L)^2](1 + \omega_b^2\tau^2)}$$

where $G_0 = \frac{I_{dc}}{V_b} = \frac{\mathcal{R}\times P_{opt}}{V_b} = 2 \cdot 10^{-4}\,\Omega^{-1}$, $G_L = \frac{1}{70}\Omega^{-1}$, $B_L = 0, C = 5$ fF, $\tau = 0.4$ ps

B1.3: Impedance matching: $G_0 = G_L \Leftrightarrow P_{opt} = G_L V_b/\mathcal{R}$

N.A : $P_{opt} = 3.57$ W ! Well beyond the thermal failure …

B2.1

Eq. 42 in p. 17.

$$P_L = \frac{1}{2}\frac{|i_c(\omega)|^2 G_L}{{G_L}^2 + (B_L + \omega C)^2}$$

Here $B_L = 0$ then $P_L = \frac{1}{2}R_L\frac{|i_c(\omega)|^2}{1+(\omega R_L C)^2}$ with $R_L = \frac{1}{G_L} = 70\ \Omega$, i_c is given in solution of **A6**.

The capacitance $C \approx \frac{\epsilon_r\epsilon_0 A}{W_c} = 3.7$ fF if $\epsilon_r = 12.5$ in InP, A=10 µm^2 and $W_c = 300$ nm.

B2.3

The internal impedance of the UTC photodiode if the serie resistance is neglected is purely capacitive, it is thus impossible to have an impedance matching with a dissipative load.

C1

$Z = 119\ \Omega$

C2

Yes. $P_{opt} = 2.1$ W instead of 3.57 W.

References

[1] A. T. Forrester, R. A. Gudmundsen, and P. O. Johnson, “Photoelectric Mixing of Incoherent Light,” *Phys. Rev.*, vol. 99, no. 6, pp. 1691–1700, 1955.

[2] A. Javan, E. A. Ballik, and W. L. Bond, “Frequency Characteristics of a Continuous-Wave He-Ne Optical Maser,” *J. Opt. Soc. Am.*, vol. 52, no. 1, pp. 96–98, Dec. 1962.

[3] B. J. Mcmurtry and A. E. Siegman, “Photomixing Experiments with a Ruby Optical Maser and a Traveling-Wave Microwave Phototube,” *Appl. Opt.*, vol. 51, no. 1, pp. 133–135, 1962.

[4] H. Inaba and A. E. Siegman, “Microwave Photomixing of Optical Maser Outputs with a PIN-Junction Photodiode,” *Proc. IRE*, vol. 50, no. 8, p. 1823, 1962.

[5] R. P. Riesz, “High Speed Semiconductor Photodiodes,” *Rev. Sci. Instrum.*, vol. 33, no. 9, p. 994, 1962.

[6] M. DiDomenico, R. H. Pantell, O. Svelto, and J. N. Weaver, “Optical Frequency Mixing in Bulk Semiconductors,” *Appl. Phys. Lett.*, vol. 1, no. 4, p. 77, 1962.

[7] P. D. Coleman, R. C. Eden, and J. N. Weaver, “Mixing and Detection of Coherent Light,” *IEEE Trans. Electron Devices*, vol. ED-11, no. 11, pp. 488–497, 1964.

[8] E. Brown and K. McIntosh, “Photomixing up to 3.8 THz in low-temperature-grown GaAs,” *Appl. Phys. Lett.*, vol. 66, no. 3, pp. 285–287, 1995.

[9] F. W. Smith, A. R. Calawa, C.-L. Chen, M. J. Manfra, and L. J. Mahoney, “New MBE buffer used to eliminate backgating in GaAs MESFETs,” *IEEE Electron Device Lett.*, vol. 9, no. 2, pp. 77–80, Feb. 1988.

[10] F. W. Smith *et al.*, “Picosecond GaAs-based photoconductive optoelectronic detectors,” *Appl. Phys. Lett.*, vol. 54, no. 10, p. 890, 1989.

[11] S. Gupta *et al.*, “Subpicosecond carrier lifetime in GaAs grown by molecular beam epitaxy at low temperatures,” *Appl. Phys. Lett.*, vol. 59, no. 25, p. 3276, Dec. 1991.

[12] H. Ito, F. Nakajima, T. Furuta, and K. Yoshino, “Photonic terahertz-wave generation using antenna-integrated uni-travelling-carrier photodiode,” *Electron. Lett.*, vol. 39, no. 25, pp. 24–25, 2003.

[13] T. Nagatsuma, H. Ito, and T. Ishibashi, “High-power RF photodiodes and their applications,” *Laser Photonics Rev.*, vol. 3, no. 1–2, pp. 123–137, Feb. 2009.

[14] T. Furuta, T. Ishibashi, Y. Matsuoka, K. Nagata, N. Shimizu, and M. Tomizawa, “Pin photodiode with improved frequency response and saturation output,” 5818096, 1998.

[15] T. Ishibashi, N. Shimizu, S. Kodama, H. Ito, T. Nagatsuma, and T. Furuta, “Uni-Traveling-Carrier Photodiodes - OSA Trends in Optics and Photonics Series,” in *Ultrafast Electronics and Optoelectronics*, 1997, vol. 13, p. UC3.

[16] T. Ishibashi, S. Kodama, N. Shimizu, and T. Furuta, “High-Speed Response of Uni-Traveling-Carrier Photodiodes,” *Jpn. J. Appl. Phys.*, vol. 36, no. Part 1, No. 10, pp. 6263–6268, Oct. 1997.

[17] M. N. Feiginov, “Analysis of limitations of tetrahertz p-i-n uni-traveling-carrier photodiodes,” *J. Appl. Phys.*, vol. 102, no. 8, p. 084510, 2007.

[18] H. Ito, S. Kodama, Y. Muramoto, T. Furuta, T. Nagatsuma, and T. Ishibashi, “High-Speed and High-Output InP–InGaAs Unitraveling-Carrier Photodiodes,” *IEEE J. Sel. Top. Quantum Electron.*, vol. 10, no. 4, pp. 709–727, Jul. 2004.

[19] P. Latzel *et al.*, “Generation of mW Level in the 300-GHz Band Using Resonant-Cavity-Enhanced Unitraveling Carrier Photodiodes,” *IEEE Trans. Terahertz Sci. Technol.*, vol. 7, no. 6, pp. 800–807, Nov. 2017.

[20] S. M. Duffy, S. Verghese, a. McIntosh, a. Jackson, a. C. Gossard, and S. Matsuura, “Accurate modeling of dual dipole and slot elements used with photomixers for coherent terahertz output power,” *IEEE Trans. Microw. Theory Tech.*, vol. 49, no. 6, pp. 1032–1038, Jun. 2001.

[21] S. Verghese, K. A. McIntosh, S. Calawa, W. F. Dinatale, E. K. Duerr, and K. A. Molvar, “Generation and detection of coherent terahertz waves using two photomixers,” *Appl. Phys. Lett.*, vol. 73, no. 26, p. 3824, Dec. 1998.

[22] M. van Exter and D. R. Grischkowsky, “Characterization of an optoelectronic terahertz beam

system," *IEEE Trans. Microw. Theory Tech.*, vol. 38, no. 11, pp. 1684–1691, 1990.
[23] I. S. Gregory *et al.*, "Continuous-wave terahertz system with a 60 dB dynamic range," *Appl. Phys. Lett.*, vol. 86, no. 20, p. 204104, May 2005.
[24] A. Roggenbuck *et al.*, "Coherent broadband continuous-wave terahertz spectroscopy on solid-state samples," *New J. Phys.*, vol. 12, no. 4, p. 043017, Apr. 2010.
[25] E. Peytavit, F. Pavanello, G. Ducournau, and J.-F. Lampin, "Highly efficient terahertz detection by optical mixing in a GaAs photoconductor," *Applied Physics Letters*, vol. 103, no. 20. American Institute of Physics, p. 201107, 12-Nov-2013.
[26] E. Rouvalis, M. Fice, C. Renaud, and A. Seeds, "Millimeter-Wave Optoelectronic Mixers Based on Uni-Traveling Carrier Photodiodes," *IEEE Trans. Microw. Theory Tech.*, vol. 60, no. 3, pp. 686–691, 2012.
[27] E. Rouvalis, M. J. Fice, C. C. Renaud, and A. J. Seeds, "Optoelectronic detection of millimetre-wave signals with travelling-wave uni-travelling carrier photodiodes," *Opt. Express*, vol. 19, no. 3, p. 2079, Jan. 2011.
[28] N. Chimot *et al.*, "Terahertz radiation from heavy-ion-irradiated In[sub 0.53]Ga[sub 0.47]As photoconductive antenna excited at 1.55 μm," *Appl. Phys. Lett.*, vol. 87, no. 19, p. 193510, Nov. 2005.
[29] B. Globisch *et al.*, "Iron doped InGaAs: Competitive THz emitters and detectors fabricated from the same photoconductor," *J. Appl. Phys.*, vol. 121, no. 5, p. 053102, Feb. 2017.
[30] R. B. Kohlhaas *et al.*, "Rhodium doped InGaAs: A superior ultrafast photoconductor," *Appl. Phys. Lett.*, vol. 112, no. 10, p. 102101, Mar. 2018.
[31] T. Göbel, D. Stanze, B. Globisch, R. J. B. Dietz, H. Roehle, and M. Schell, "Telecom technology based continuous wave terahertz photomixing system with 105 decibel signal-to-noise ratio and 35 terahertz bandwidth," *Opt. Lett.*, vol. 38, no. 20, p. 4197, Oct. 2013.
[32] B. Globisch, R. J. B. Dietz, D. Stanze, T. Göbel, and M. Schell, "Carrier dynamics in Beryllium doped low-temperature-grown InGaAs/InAlAs," *Appl. Phys. Lett.*, vol. 104, no. 17, pp. 1–5, 2014.
[33] J. Mangeney, F. Meng, D. Gacemi, E. Peytavit, J. F. Lampin, and T. Akalin, "CW THz generation by In<inf>0.53</inf>Ga<inf>0.47</inf>As photomixer with TEM-Horn antenna driven at 1.55 μm wavelengths," in *IRMMW-THz 2010 - 35th International Conference on Infrared, Millimeter, and Terahertz Waves, Conference Guide*, 2010.
[34] J. Mangeney, A. Merigault, N. Zerounian, P. Crozat, K. Blary, and J. F. Lampin, "Continuous wave terahertz generation up to 2 THz by photomixing on ion-irradiated In[sub 0.53]Ga[sub 0.47]As at 1.55 μm wavelengths," *Appl. Phys. Lett.*, vol. 91, no. 24, p. 241102, 2007.
[35] R. A. Mohandas *et al.*, "Generation of continuous wave terahertz frequency radiation from metal-organic chemical vapour deposition grown Fe-doped InGaAs and InGaAsP," *J. Appl. Phys.*, vol. 119, no. 15, p. 153103, Apr. 2016.
[36] J. E. Bjarnason *et al.*, "ErAs:GaAs photomixer with two-decade tunability and 12 μW peak output power," *Appl. Phys. Lett.*, vol. 85, no. 18, pp. 3983–3985, 2004.
[37] E. Peytavit *et al.*, "Continuous terahertz-wave generation using a monolithically integrated horn antenna," *Appl. Phys. Lett.*, vol. 93, no. 11, p. 111108, 2008.
[38] S. Verghese, K. A. Mcintosh, and E. R. Brown, "Optical and terahertz power limits in the low-temperature-grown GaAs photomixers," *Appl. Phys. Lett.*, vol. 71, no. November, pp. 2743–2745, 1997.
[39] H. Ito, T. Furuta, S. Kodama, and T. Ishibashi, "InP/InGaAs uni-travelling-carrier photodiode with 310 GHz bandwidth," *Electron. Lett.*, vol. 36, no. 21, p. 1809, 2000.
[40] H. Ito *et al.*, "High-power photonic millimetre wave generation at 100 GHz using matching-circuit-integrated uni-travelling-carrier photodiodes," *IEE Proc. - Optoelectron.*, vol. 150, no. 2, p. 138, 2003.
[41] F. Nakajima, T. Furuta, and H. Ito, "High-power continuous-terahertz-wave generation using resonant-antenna-integrated uni-travelling-carrier photodiode," *Electron. Lett.*, vol. 40, no. 20, pp. 3–4, 2004.

[42] A. Beck *et al.*, “High-efficiency uni-travelling-carrier photomixer at 1.55 µm and spectroscopy application up to 1.4 THz,” *Electron. Lett.*, vol. 44, no. 22, p. 1320, 2008.

[43] A. Wakatsuki, T. Furuta, Y. Muramoto, T. Yoshimatsu, and H. Ito, “High-power and broadband sub-terahertz wave generation using a J-band photomixer module with rectangular-waveguide output port,” in *2008 33rd International Conference on Infrared, Millimeter and Terahertz Waves*, 2008, pp. 1–2.

[44] E. Rouvalis, C. C. Renaud, D. G. Moodie, M. J. Robertson, and A. J. Seeds, “Continuous Wave Terahertz Generation From Ultra-Fast InP-Based Photodiodes,” *IEEE Trans. Microw. Theory Tech.*, vol. 60, no. 3, pp. 509–517, Mar. 2012.

[45] E. Rouvalis, C. C. Renaud, D. G. Moodie, M. J. Robertson, and A. J. Seeds, “Traveling-wave Uni-Traveling Carrier photodiodes for continuous wave THz generation.,” *Opt. Express*, vol. 18, no. 11, pp. 11105–10, May 2010.

[46] I. D. Henning *et al.*, “Broadband Antenna-Integrated, Edge-Coupled Photomixers for Tuneable Terahertz Sources,” *IEEE J. Quantum Electron.*, vol. 46, no. 10, pp. 1498–1505, Oct. 2010.

[47] P. D. Yoder and E. J. Flynn, “Quasi-unipolar InGaAs⁄InP photodetection for enhanced optical saturation power and maximal bandwidth,” *Appl. Phys. Lett.*, vol. 91, no. 6, p. 062114, Aug. 2007.

[48] J. Farhoomand and R. E. McMurray, “Design parameters of a resonant infrared photoconductor with unity quantum efficiency,” *Appl. Phys. Lett.*, vol. 58, no. 6, p. 622, Feb. 1991.

[49] K. Kishino, M. S. Unlu, J.-I. Chyi, J. Reed, L. Arsenault, and H. Morkoc, “Resonant cavity-enhanced (RCE) photodetectors,” *IEEE J. Quantum Electron.*, vol. 27, no. 8, pp. 2025–2034, 1991.

[50] N. Li *et al.*, “High Power Photodiode Wafer Bonded to Si Using Au With Improved Responsivity and Output Power,” vol. 18, no. 23, pp. 2526–2528, 2006.

[51] E. Peytavit and J.-F. Lampin, “Photomelangeur pour la generation de rayonnement terahertz,” WO2011030011 A3, 2010.

[52] E. Peytavit, C. Coinon, and J.-F. Lampin, “A metal-metal Fabry–Pérot cavity photoconductor for efficient GaAs terahertz photomixers,” *J. Appl. Phys.*, vol. 109, no. 1, p. 016101, 2011.

[53] E. D. Palik, *Handbook of Optical Constants of Solids, Volume 3*. Academic Press, 1998.

[54] A. Yariv and P. Yeh, *Photonics: Optical Electronics in Modern Communications*. Oxford University Press, 2006.

[55] E. Peytavit, C. Coinon, and J.-F. Lampin, “Low-Temperature-Grown GaAs Photoconductor with High Dynamic Responsivity in the Millimeter Wave Range,” *Appl. Phys. Express*, vol. 4, no. 10, p. 104101, Sep. 2011.

[56] E. Peytavit, P. Latzel, F. Pavanello, G. Ducournau, and J.-F. Lampin, “Milliwatt output power generated in the J-Band by a GaAs photomixer,” in *Proceedings of 38th International Conference on Infrared, Millimeter and Terahertz Waves, IRMMW-THz*, 2013, pp. 1–3.

[57] E. Peytavit *et al.*, “Milliwatt-level output power in the sub-terahertz range generated by photomixing in a GaAs photoconductor,” *Appl. Phys. Lett.*, vol. 99, no. 22, p. 223508, 2011.

[58] E. Peytavit, P. Latzel, F. Pavanello, G. Ducournau, and J.-F. Lampin, “CW Source Based on Photomixing With Output Power Reaching 1.8 mW at 250 GHz,” *IEEE Electron Device Lett.*, vol. 34, no. 10, pp. 1277–1279, Oct. 2013.

[59] S. Demiguel, J. C. Campbell, D. Tulchinsky, and K. J. Williams, “A comparison of front- and backside-illuminated high-saturation power partially depleted absorber photodetectors,” *IEEE J. Quantum Electron.*, vol. 40, no. 9, pp. 1321–1325, Sep. 2004.

[60] T. Ishibashi, Y. Muramoto, T. Yoshimatsu, and H. Ito, “Unitraveling-Carrier Photodiodes for Terahertz Applications,” *IEEE J. Sel. Top. Quantum Electron.*, vol. 20, no. 6, pp. 79–88, Nov. 2014.

[61] F. J. Garcia-Vidal, L. Martin-Moreno, T. W. Ebbesen, and L. Kuipers, “Light passing through subwavelength apertures,” *Rev. Mod. Phys.*, vol. 82, no. 1, pp. 729–787, Mar. 2010.

[62] K. J. Williams and R. D. Esman, “Design Considerations for High-Current Photodetectors,” *J.*

Light. Technol. Vol. 17, Issue 8, pp. 1443-, vol. 17, no. 8, p. 1443, Aug. 1999.
[63] R. Mendis, C. Sydlo, J. Sigmund, M. Feiginov, P. Meissner, and H. L. Hartnagel, "Spectral Characterization of Broadband THz Antennas by Photoconductive Mixing: Toward Optimal Antenna Design," *IEEE Antennas Wirel. Propag. Lett.*, vol. 4, no. 1, pp. 85–88, Dec. 2005.
[64] S. Matsuura, M. Tani, and K. Sakai, "Generation of coherent terahertz radiation by photomixing in dipole photoconductive antennas," *Appl. Phys. Lett.*, vol. 70, no. 5, p. 559, Feb. 1997.
[65] K. McIntosh, E. Brown, and K. Nichols, "Terahertz measurements of resonant planar antennas coupled to low-temperature-grown GaAs photomixers," *Appl. Phys. Lett.*, vol. 69, no. December, pp. 3632–3634, 1996.
[66] V. Rumsey, "Frequency independent antennas," in *IRE International Convention Record*, 1957, vol. 5, pp. 114–118.
[67] V. Rumsey, *Frequency independent antennas*, Academic P. New York, 1966.
[68] J. D. Kraus, "Antennas," McGraw-Hil., New York, 1950.
[69] J. Dyson, "The equiangular spiral antenna," *Antennas Propagation, IRE Trans.*, vol. 7, no. 2, pp. 181–187, 1959.
[70] R. DuHamel and D. Isbell, "Broadband logarithmically periodic antenna structures," in *IRE International Convention Record*, 1957, vol. 5, pp. 119–128.
[71] I. S. Gregory *et al.*, "Optimization of photomixers and antennas for continuous-wave terahertz emission," *IEEE J. Quantum Electron.*, vol. 41, no. 5, pp. 717–728, May 2005.
[72] M. Ravaro *et al.*, "Phase-locking of a 25 THz quantum cascade laser to a frequency comb using a GaAs photomixer," *Opt. Lett.*, vol. 36, no. 20, p. 3969, Oct. 2011.
[73] E. Peytavit, T. Akalin, J.-F. Lampin, F. Hindle, C. Yang, and G. Mouret, "THz photomixing: Comparison between horn and spiral antennas," in *2009 34th International Conference on Infrared, Millimeter, and Terahertz Waves*, 2009, pp. 1–3.
[74] H. Ito and T. Ishibashi, "Photonic Terahertz-Wave Generation Using Slot-Antenna-Integrated Uni-Traveling-Carrier Photodiodes," *IEEE J. Sel. Top. Quantum Electron.*, vol. 23, no. 4, pp. 1–7, Jul. 2017.
[75] D. B. Rutledge, D. P. Neikirk, and D. P. Kasilingam, "Integrated circuits antennas," in *Infrared and millimeter waves, Vol.10*, K. J. Button, Ed. New York: Academic Press, 1983, pp. 1–90.
[76] D. P. Neikirk, "Far-infrared imaging antenna arrays," *Appl. Phys. Lett.*, vol. 40, no. 3, p. 203, Feb. 1982.
[77] C. Fattinger and D. Grischkowsky, "Terahertz beams," *Appl. Phys. Lett.*, vol. 54, no. 6, p. 490, Feb. 1989.
[78] P. U. Jepsen and S. R. Keiding, "Radiation patterns from lens-coupled terahertz antennas," *Opt. Lett.*, vol. 20, no. 8, p. 807, Apr. 1995.
[79] L. Liu, J. L. Hesler, H. Xu, A. W. Lichtenberger, and R. M. Weikle, "A Broadband Quasi-Optical Terahertz Detector Utilizing a Zero Bias Schottky Diode," *IEEE Microw. Wirel. Components Lett.*, vol. 20, no. 9, pp. 504–506, Sep. 2010.
[80] I. C. Mayorga, "Photomixer as tunable terahertz local oscillators," Bonn, 2008.
[81] C. Sydlo, J. Sigmund, H. L. Hartnagel, G. Loata, K. J. Siebert, and H. G. Roskos, "Efficient THz-emitters for low-temperature-grown GaAs photomixers," in *Proceedings, IEEE Tenth International Conference on Terahertz Electronics*, pp. 60–62.
[82] A. Beck, T. Akalin, G. Ducournau, E. Peytavit, and J.-F. Lampin, "Terahertz photomixers based on ultra-wideband horn antennas," *Comptes Rendus Phys.*, vol. 11, no. 7–8, pp. 472–479, Aug. 2010.
[83] L. Prissette *et al.*, "Radiation Pattern Measurements of an Integrated Transverse Electromagnetic Horn Antenna Using a Terahertz Photomixing Setup," *IEEE Microw. Wirel. Components Lett.*, vol. 21, no. 1, pp. 49–51, Jan. 2011.
[84] "https://www.anritsu.com/en-us/test-measurement/news/news-releases/2019/2019-05-31-us01." .
[85] "https://vadiodes.com/VDI/pdf/waveguidechart200908.pdf." .

[86] “https://www.formfactor.com/product/probes/infinity/infinity-waveguide-probe/.” .
[87] “Picoprobes for wafer-level testing.” [Online]. Available: http://www.ggb.com/.
[88] T. Reck, L. Chen, and C. Zhang, “Micromachined probes for submillimeter-wave on-wafer measurements—Part I: Mechanical design and characterization,” *IEEE Trans. Terahertz Sci. Technol.*, vol. 1, no. 2, pp. 349–356, 2011.
[89] “T-waves probes, Form Factor company.”
[90] T. J. Reck *et al.*, “Micromachined on-wafer probes,” in *2010 IEEE MTT-S International Microwave Symposium*, 2010, pp. 65–68.
[91] P. Latzel *et al.*, “Generation of mW Level in the 300-GHz Band Using Resonant-Cavity-Enhanced Unitraveling Carrier Photodiodes,” *IEEE Trans. Terahertz Sci. Technol.*, vol. 7, no. 6, pp. 800–807, Nov. 2017.
[92] “https://www.ptb.de/cms/en/presseaktuelles/journals-magazines/ptb-news/ptb-news-ausgaben/archivederptb-news/ptb-news-2014-2/detector-standard-for-terahertz-radiation.html.” .
[93] Z. Popovic and E. N. Grossman, “THz Metrology and Instrumentation,” *IEEE Trans. Terahertz Sci. Technol.*, vol. 1, no. 1, pp. 133–144, Sep. 2011.
[94] “Quasi-optic detector from VDI Inc.” [Online]. Available: https://www.vadiodes.com/VDI/pdf/2009AugustNews.pdf.